

Structure of *C. elegans* TMC-1 complex illuminates auditory mechanosensory transduction

Eric Gouaux (✉ gouauxe@ohsu.edu)

OHSU <https://orcid.org/0000-0002-8549-2360>

Sarah Clark

OHSU

Hanbin Jeong

April Goehring

Oregon Health and Science University

Sepehr Dehghani-Ghahnaviyeh

University of Illinois at Urbana-Champaign

Ali Rasouli

University of Illinois

Emad Tajkhorshid

University of Illinois at Urbana-Champaign <https://orcid.org/0000-0001-8434-1010>

Biological Sciences - Article

Keywords:

Posted Date: May 6th, 2022

DOI: <https://doi.org/10.21203/rs.3.rs-1623715/v1>

License:  This work is licensed under a Creative Commons Attribution 4.0 International License.

[Read Full License](#)

Version of Record: A version of this preprint was published at Nature on October 12th, 2022. See the published version at <https://doi.org/10.1038/s41586-022-05314-8>.

1 5.4.22

2

3

4 **Structure of *C. elegans* TMC-1 complex illuminates auditory mechanosensory transduction**

5

6 Hanbin Jeong^{1*}, Sarah Clark^{1*}, April Goehring^{1,2}, Sepehr Dehghani-Ghahnaviyeh³, Ali Rasouli³, Emad,

7

Tajkhorshid³ and Eric Gouaux^{1,2}

8

1. Vollum Institute, Oregon Health & Science University, Portland, Oregon 97239, USA.

9

2. Howard Hughes Medical Institute, Oregon Health & Science University, Portland, Oregon 97239,

10

USA.

11

3. Theoretical and Computational Biophysics Group, NIH Center for Macromolecular Modeling and

12

Bioinformatics, Beckman Institute for Advanced Science and Technology, Department of Biochemistry,

13

and Center for Biophysics and Quantitative Biology, University of Illinois at Urbana-Champaign, Urbana,

14

Illinois 61801, USA.

15

*These authors made equal contributions.

16

Correspondence to Eric Gouaux: gouauxe@ohsu.edu

17

18 Summary

19 The initial step in the sensory transduction pathway underpinning hearing and balance in mammals involves
20 the conversion of force into the gating of a mechanosensory transduction (MT) channel. Despite the
21 profound socioeconomic impacts of hearing disorders and the fundamental biological significance of
22 understanding MT, the composition, structure and mechanism of the MT complex has remained
23 elusive. Here we report the single particle cryo-EM structure of the native MT TMC-1 complex isolated
24 from *C. elegans*. The 2-fold symmetric complex is composed of 2 copies each of the pore-forming TMC-1
25 subunit, the calcium-binding protein CALM-1 and the transmembrane inner ear protein TMIE. CALM-1
26 makes extensive contacts with the cytoplasmic face of the TMC-1 subunits while the single-pass TMIE
27 subunits reside on the periphery of the complex, poised like the handles of an accordion. A subset of
28 particles in addition harbors a single arrestin-like protein, ARRD-6, bound to a CALM-1 domain. Single-
29 particle reconstructions and molecular dynamics simulations show how the MT complex deforms the
30 membrane bilayer and suggest crucial roles for lipid-protein interactions in the mechanism by which
31 mechanical force is transduced to ion channel gating.

32 Main

33 The auditory system is endowed with a remarkable ability to detect a wide range of acoustic wave
34 frequencies and amplitudes by transducing vibrational mechanical energy into membrane potential
35 depolarization, followed by signal processing in higher brain centers, thus enabling the sensation of sound¹.
36 Dysfunction of the auditory system, from injury, environmental insult or genetic mutation, is associated
37 with age-related hearing loss. Hearing impairment and deafness impacts over 460 million individuals
38 worldwide, with an estimated annual cost of unaddressed hearing loss at \$750-790 billion². Input into the
39 auditory and the closely related vestibular system, like other sensory systems, is initiated by receptor
40 activation on peripheral neurons. Despite intense investigation over several decades, the molecular
41 composition, structure and mechanism of the receptor for mechanosensory transduction, deemed the MT
42 complex, has remained unresolved.

43 Multiple lines of investigation from studies on humans and model organisms including mice,
44 zebrafish and *C. elegans*, nevertheless, have shed light on the proteins that form the MT complex and their
45 likely roles in its function³. These include the tip link proteins, protocadherin-15 and cadherin-23, that in
46 hair cells transduce the force derived from stereocilia displacement to the opening of the ion channel
47 component of the MT complex^{4,5}. The transmembrane ion channel like proteins 1 and 2 (TMC-1 and TMC-
48 2) are the likely pore-forming subunits of the MT complex, candidates that first came to prominence from
49 human genetic studies⁶, and more recently gained traction as the ion conduction pathway via biophysical
50 and biochemical investigations^{7,8}. Additional proteins, some of which may be ‘auxiliary subunits’, have
51 been associated with either the biogenesis or function of the MT complex and include transmembrane inner
52 ear protein (TMIE)⁹⁻¹¹, Ca²⁺ and integrin binding protein 2 (CIB2)¹²⁻¹⁴, lipoma HMGIC fusion-like protein
53 5 (LHFPL5)¹⁵⁻¹⁷, transmembrane O-methyl transferase (TOMT)^{18,19} and possibly ankyrin¹³.

54 Isolation of the MT complex from vertebrate sources or production of a functional complex via
55 recombinant methods have proven unsuccessful. Complex purification from native sources is particularly
56 challenging due to the small number of complexes per animal, estimated as $\sim 3 \times 10^6$ per mammalian cochlea
57 ²⁰, miniscule compared to the number of photoreceptors of the visual system, which is $\sim 4 \times 10^{14}$ per murine

58 eye²¹. To surmount challenges with vertebrate MT complex availability, we turned to *C. elegans*, an animal
59 that harbors a MT complex used for sensing tactile stimuli. We note first that *C. elegans* expresses crucial
60 components of the vertebrate MT complex, including the TMC-1 and TMC-2 proteins, in addition to a
61 CIB2 homolog, known as CALM-1, as well as TMIE¹³. Second, worms that are devoid of TMC-1 exhibit
62 attenuated light touch responses¹³. Third, despite the limited expression of the TMC proteins in *C. elegans*,
63 it is feasible to grow a sufficient number of worms to isolate enough complex for structural studies. We
64 thus modified the *C. elegans tmc-1* locus by including a fluorescent reporter and an affinity tag, thereby
65 allowing us to monitor expression via whole animal fluorescence and fluorescence-detection size-exclusion
66 chromatography (FSEC)²², and to isolate the TMC-1 complex by affinity chromatography. Together with
67 computational studies, we elucidated the composition, architecture and membrane interactions of the
68 complex, and suggest mechanisms for gating of the ion channel pore by both direct protein interactions and
69 via the membrane bilayer.

70 **TMC-1 complex is a dimer**

71 We generated a transgenic knock-in worm line where a nucleic acid sequence encoding an mVenus-
72 3xFLAG tag was inserted at the 3' end of the TMC-1 coding sequence, immediately before the stop codon
73 (Supplementary Fig. 1). The engineered, homozygous worm line, deemed *tmc-1::mVenus*, was
74 characterized by spectral confocal imaging, revealing mVenus fluorescence in the head and tail neurons,
75 and in body wall and vulval muscles (Fig. 1a), consistent with previous studies demonstrating expression
76 of TMC-1 in these cells²³. The TMC-1 complex was isolated from the *tmc-1::mVenus* transgenic worms
77 by affinity chromatography and further purified by size exclusion chromatography (SEC) (Fig. 1b). The
78 estimated molecular weight of the TMC-1 complex by SEC is ~780 kDa, suggesting that the complex
79 harbors multiple TMC-1 protomers and perhaps additional, auxiliary subunits.

80 To independently interrogate the oligomeric state of the complex, we performed single molecule
81 pulldown (SiMPull) experiments²⁴. Photobleaching traces of captured TMC-1 complexes demonstrate that
82 ~62% of the mVenus fluorophores bleached in two steps, 37% bleached in one step, and 1% bleached in
83 three steps (Fig. 1c; Extended Data Fig. 1), consistent with the conclusion that within the TMC-1 complex

84 there are two copies of the TMC-1 subunit. The discrepancy between the predicted ~300 kDa molecular
85 weight of a *C. elegans* TMC-1 dimer and the molecular weight of the complex estimated by SEC points
86 towards the presence of auxiliary proteins. As several TMC-1 binding partners have been identified in
87 worms¹³ and in vertebrates³, we next probed the composition of the TMC-1 complex using mass
88 spectrometry (MS).

89 MS analysis of the TMC-1 complex identified three proteins that co-purified with TMC-1: (1)
90 CALM-1, an ortholog of mammalian Ca²⁺ and integrin-binding family member 2 (CIB2); (2) an ortholog
91 of mammalian transmembrane inner ear expressed protein (TMIE); (3) ARRestin domain protein (ARRD-
92 6), an ortholog of the mammalian arrestin-domain-containing family of proteins (Fig. 1d; Extended Data
93 Fig. 2). All three proteins were found in the TMC-1 sample purified from transgenic worms but not in the
94 control sample prepared from wild-type worms, consistent with their specific association with the TMC-1
95 complex. The mammalian ortholog of CALM-1 is CIB2, and CIB2 which together with TMIE are likely
96 components of the mammalian MT complex, localize to stereocilia^{9-12,14,25} and bind to heterologously
97 expressed TMC-1 fragments through pull-down assays¹⁰. By contrast, ARRD-6 has not been described as
98 a component of either the *C. elegans* or vertebrate TMC-1 complexes. Despite repeated efforts, we found
99 no evidence for the presence of UNC-44, the worm ortholog of mammalian ankyrin, in contrast with a
100 previous report that UNC-44 forms a complex with CALM-1, is necessary for TMC-1 mediated
101 mechanotransduction, and is the 'gating spring' of the TMC-1 complex¹³, thus raising the question of the
102 role of UNC-44 and by extension ankyrin to the structure and function of MT complexes in worms and
103 vertebrates, respectively.

104 **Overall architecture of the TMC-1 complex**

105 To elucidate the architecture and arrangement of subunits in the TMC-1 complex, we performed
106 single particle cryo-electron microscopy (cryo-EM). TMC-1 is expressed at a low level in *C. elegans* and
107 therefore approximately 6×10^7 transgenic worms were required to yield ~50 ng of TMC-1 complex for
108 cryo-EM analysis. The TMC-1 complex was visualized on 2 nm carbon-coated grids that were glow
109 discharged in the presence of amylamine. Cryo-EM imaging revealed a near ideal particle distribution and

110 we proceeded to collect a dataset comprised of 26,055 movies. Reference-free 3D classification
111 reconstruction, together with refinements, resulted in three well-defined classes (Extended Data Figs. 3- 5,
112 Extended Data Table 1). Two of these classes represent the TMC-1 complex in different conformational
113 states, deemed the ‘Expanded’ (E) and ‘Contracted’ (C) conformations, both of which exhibit an overall
114 resolution of 3.1 Å (Extended Data Figs. 3 and 5). A third class includes the auxiliary subunit ARRD-6 and
115 was resolved at 3.5 Å resolution (Extended Data Fig. 4 and 5, Extended Data Table 1). Because the ‘E’
116 conformation has a few more distinct density features than the ‘C’ conformation, we will focus on the ‘E’
117 conformation in our initial discussion of the overall structure.

118 The TMC-1 complex is dimeric in subunit stoichiometry, with a 2-fold axis of rotational symmetry
119 centered at a site of contacts between the two TMC-1 subunits (Fig. 2). The transmembrane helices exhibit
120 better local resolution than average, while disordered or dynamic peripheral components of the complex
121 are resolved at lower resolution (Fig. 2b). When viewed perpendicular to the membrane plane, the complex
122 has the shape of a ‘figure 8’, with TMC-1 subunits centered within the lobes of the ‘8’ (Fig. 2d). Each
123 TMC-1 protomer consists of ten transmembrane helices with an overall arrangement that is reminiscent of
124 the Ca²⁺-activated lipid scramblase ²⁶, TMEM16 Cl⁻ channels ^{27,28} and OSCA mechanosensitive ion
125 channels ^{29,30} (Extended Data Fig. 6). At the juncture of the figure ‘8’ lobes, the dimer interface is composed
126 of domain-swapped TM10 helices (Fig. 2e), with contacts defined by van der Waals and electrostatic
127 interactions, and by burial of 1,781 Å² of solvent accessible surface area. Numerous well-ordered lipid
128 molecules surround the transmembrane domain, many of which are intercalated in the grooves between
129 transmembrane helices, and some of which are positioned at a large angle to the membrane plane.

130 Poised to make extensive interactions with the inner leaflet of the membrane, the cytosolic domain
131 harbors six helices oriented nearly parallel to the membrane. The two helices located closest to inner leaflet,
132 H3 and H4, are amphipathic, a common feature among mechanosensitive ion channels ³¹ (Fig. 2c, d). The
133 short linker between TMC-1 H3 and H4 is composed of nonpolar residues that interact with the inner leaflet
134 membrane, forming hydrophobic contacts with the acyl chains of two lipids. The ~400-residue, cytosolic
135 C-terminus of TMC-1, which is predicted to be partially structured, was not visible in the cryo-EM map.

136 Because MS analysis of the purified MT complex identified nine peptides that spanned the entirety of the
137 C-terminus, we suspect that this region is intact in the TMC-1 complex, but not visible due to
138 conformational heterogeneity (Extended Data Fig. 2 legend).

139 Three partially structured loops decorate the extracellular side of the TMC-1 complex. Two of the
140 loops are ~60 residues in length, bridging TM1/TM2 and TM9/TM10, and are well-conserved between
141 vertebrate and *C. elegans* TMC-1. Density features consistent with glycosylation can be found at N209,
142 located in the loop between TM1 and TM2. By contrast, the ~200-residue extracellular loop that connects
143 TM5 and TM6 was not observed in the cryo-EM map. We detected two peptides from this region in the
144 MS analysis (Extended Data Fig. 2 legend), indicating that the loop is present but not visible due to
145 flexibility. This region is predicted to contain elements of secondary structure, as well as three predicted
146 sites of *N*-linked glycosylation, but its function is unclear. The loop is not well conserved between TMC-1
147 and TMC-2, and its length in vertebrate TMC-1, at ~50 residues, is substantially shorter.

148 Two additional subunits, CALM-1 and TMIE, present in two copies each, complete the ensemble
149 of proteins associated with the ‘core’ TMC-1 complex. The quality of the cryo-EM map enabled
150 unambiguous assignment of CALM-1 and TMIE auxiliary subunits (Fig. 2c) to density features of the
151 TMC-1 complex map, in accord with the MS data. The CALM-1 subunits ‘grip’ the cytosolic faces of each
152 TMC-1 protomer while each of the two TMIE subunits span the membrane, nearly ‘floating’ on the
153 periphery of complex, flanking each TMC-1 subunit. CALM-1 makes extensive contacts with five of the
154 six cytosolic helices, forming a ‘cap’ at the base of the TMC-1 transmembrane domain. By contrast, the
155 TMIE subunits define the distal edges of the complex, participating in only a handful of protein-protein
156 contacts on the extracellular and cytosolic boundaries of the membrane spanning regions, but with lipid
157 mediated interactions through the transmembrane regions. Viewed parallel to the membrane and
158 perpendicular to the long face of the complex, the arrangement of subunits resembles an accordion, with
159 the TMIE transmembrane helices forming the instrument handles and the TMC-1 transmembrane domain
160 defining the bellows (Fig. 2c).

161 **Extensive lipid-mediated interactions of TMIE with TMC-1**

162 TMIE is an essential subunit of the vertebrate MT complex that is necessary for TMC-1 mediated
163 MT in cochlear hair cells² and in zebrafish sensory hair cells¹⁰. Multiple point mutations in TMIE are
164 linked to deafness (Extended Data Fig. 7), and recent studies suggest a role for TMIE in TMC-1/2
165 localization and channel gating^{9-11,32-34}. The *C. elegans* TMC-1 complex contains two copies of TMIE
166 located on the ‘outside’ of each TMC-1 protomer (Fig. 3a). TMIE consists of a single transmembrane
167 domain followed by an ‘elbow-like’ linker and a cytosolic helix (Fig. 3b). The flexible, positively charged
168 C-terminal tail was not visible in the cryo-EM map. The interaction between TMIE and TMC-1 is mediated
169 primarily by the cytosolic TMIE elbow, with the highly conserved R49 and R52 forming hydrogen bonds
170 with backbone carbonyl atoms in TMC-1 TM6 and TM8, respectively (Fig. 3c, e). These arginine residues
171 can be mapped to known deafness mutations in humans (R81C and R84W), highlighting the importance of
172 these hydrogen bonds in the TMIE/TMC-1 interaction. Hydrophobic contacts between non-polar residues
173 in the TMIE elbow and TMC-1 TM6 likely strengthen the complex. Additionally, W25 of TMIE, near the
174 extracellular boundary, contacts L228 in the loop between TMC-1 TM1 and TM2 (Fig. 3d). Mutation of
175 the corresponding residue in humans (W57) to a stop codon is a cause of deafness³⁵. We did not observe
176 density for the N-terminal 17 residues of TMIE in the cryo-EM map and peptides from this region were not
177 detected in the MS analysis, suggesting that the N-terminus contains a cleaved signal peptide
178 (Supplementary Fig. 2). N-terminal sequencing of recombinantly expressed murine TMIE is also consistent
179 with cleavage of a signal peptide (Supplementary Fig. 2), as are truncation experiments of zebrafish TMIE
180¹⁰, supporting the hypothesis that in *C. elegans* the first ~17 residues of TMIE functions as a signal peptide.

181 There is a striking intramembranous ‘cavity’ between TMIE and TMC-1 that is occupied by at least
182 eight lipid molecules. Several lipids make hydrophobic contacts with nonpolar residues in TMIE and the
183 putative pore-forming TMC-1 helices TM6 and TM8, bridging the two subunits. Consistent with the
184 observed lipid density in the cryo-EM maps, molecular dynamics (MD) simulations independently identify
185 multiple lipids in this cavity (Extended Data Fig. 9). Notably, C44 of TMIE on the cytosolic boundary of
186 the transmembrane domain is palmitoylated, with the acyl chain extending along TMC-1 TM8 (Fig. 3d, e).
187 The location of TMIE near the putative TMC-1 pore and its lipid interactions suggests roles for TMIE, and

188 possibly lipids, in gating by sensing membrane tension. This idea is supported by recent studies in mouse
189 cochlear hair cells, which demonstrated that TMIE binds to phospholipids and its association with lipids is
190 important for TMC-1 MT¹¹.

191 **CALM-1 subunits cloak cytoplasmic surfaces of TMC-1**

192 Calcium and integrin-binding protein 2 (CIB2) and its homolog, CIB3, modulate the activity of the
193 MT complex and bind to the TMC-1 subunit^{12,14}. In harmony with the role of CIB2/CIB3 in MT channel
194 function, mutants of CIB2 are associated with non-syndromic hearing loss^{25,36,37}. Our MS results (Fig. 1d
195 and Extended Data Fig. 2) demonstrate that CALM-1, the *C. elegans* ortholog of CIB2, co-purifies with
196 TMC-1, consistent with CALM-1 residing within the TMC-1 complex. Inspection of the map of the TMC-
197 1 complex reveals density features for two CALM-1 subunits on the cytosolic faces of each TMC-1
198 protomer. By exploiting the crystal structure of CIB3 in complex with a TMC-1 peptide¹⁴, we fit models
199 of CALM-1 to their respective density features (Fig. 4a). Like other CIB proteins, CALM-1 has three EF-
200 hand motifs, two of which are located proximal to the C-terminus and harbor clearly bound Ca²⁺ ions.
201 Following superposition, the root-mean-square deviation (RMSD) between CALM-1 and CIB3 from the
202 CIB3-TMC-1 peptide complex is 0.69 Å, and together with a substantial sequence similarity, underscore
203 the conservation of sequence and structure between the worm and mouse proteins (Extended Data Fig. 8).

204 Extensive interactions knit together CALM-1 and TMC-1, involving a buried surface area of
205 ~2,903 Å², and suggesting that CALM-1 may bind to TMC-1 with high affinity (Fig. 4a). Three distinct
206 regions of CALM-1 interact with cytosolic helical features of TMC-1, the first of which involves TMC-1
207 helices H1 to H3, oriented like ‘paddles’ nearly parallel to the membrane (Fig. 4b, c). Prominent interactions
208 include side chains in the loop between H1 and H2, which form hydrophobic contacts with CALM-1,
209 together with acidic residues on CALM-1 that create a negatively charged surface juxtaposed to a
210 complementary positively charged surface on the H1-H3 paddle (Fig. 4c). The second binding interface is
211 through a hydrophobic pocket of CALM-1, comprised of its EF-hand motifs, and the cytosolic H5-H6
212 helices of TMC-1 (Fig. 4d), reminiscent of the CIB3/TMC-1 peptide structure. Aliphatic and aromatic
213 residues, including L308, F309 and Y314 of TMC-1 are docked into the conserved hydrophobic core in

214 CALM-1, further stabilizing the complex by burial of substantial non-polar surface area. Lastly, amino
215 acids D192, R195 and R200 at the C-terminus of CALM-1 interact with R780, D313 and E160 of TMC-1,
216 respectively, forming conserved salt bridges through the buried short helix (191-197) of CALM-1 (Fig. 4e).
217 This interface shows that CALM-1 directly engages with the transmembrane helices of TMC-1 via the loop
218 between TM8 and TM9, and is thus positioned to modulate the ion channel function.

219 Multiple missense mutations of human CIB2 or TMC-1 are associated with non-syndromic hearing
220 loss by either impeding the interaction between TMC-1 and CIB2 or by reducing the Ca^{2+} binding
221 propensity of CIB2¹⁴. Several of these residues, E178D of human TMC-1 and E64D, F91S, Y115C, I123T,
222 and R186W of CIB2, are structurally conserved in the *C. elegans* TMC-1 and CALM-1 complex (Extended
223 Data Fig. 8). Our structure illuminates the proximity of the CALM-1 Ca^{2+} binding sites to the CALM-1 and
224 TMC-1 interface, thus underscoring the roles of both Ca^{2+} and CALM-1 in sculpting the conformation of
225 the TMC-1 and by extrapolation, providing a structural understanding of CIB2 in hair cell function.

226 MS analysis of the TMC-1 complex indicated the presence of a soluble protein known as ARRD-
227 6. Upon classification of the single particle cryo-EM data, we noticed one, non 2-fold symmetric, 3D class
228 defined by an elongated density feature protruding from the CALM-1 auxiliary subunit and we
229 hypothesized that it could correspond to ARRD-6. Arrestins are composed of an N- and a C- domain, each
230 comprised of β -sandwich motifs, which together give rise to a protein with an elongated, bean-like shape.
231 We fit the predicted structure of ARRD-6 into the corresponding density feature and although the local
232 resolution of the ARRD-6 region is lower than that of central region of the complex, the fit yielded overall
233 correlation coefficients of 0.69 (mask) and 0.65 (volume) (Extended Data Fig. 5). Moreover, density
234 features for the ARRD-6 β -sheets are clearly observed at the binding interface with CALM-1, as well as
235 for the crossed elongated loops of the N- and C-domain at the central crest, further supporting the
236 assignment of the density feature to ARRD-6. We observed a ‘C-edge loop’ structure, positioned at the
237 distal edge of the β -strands in the C-domain, a feature which functions as a membrane anchor and is
238 necessary for activation of arrestin (Fig. 4f, g)³⁸. The C-edge loop of ARRD-6 includes W197 and multiple

239 cysteine residues (Fig. 4g), the latter of which may be palmitoylated and thus poised for membrane
240 anchoring³⁹. Additional contacts between CALM-1 and ARRD-6 involve a loop of CALM-1 (P51-K67)
241 with the β -strands in the C-domain of ARRD-6 (Fig. 4h). At present, there is no known role for an arrestin
242 in the function of the TMC channel of *C. elegans*, nor in the vertebrate TMC-1 complex. We speculate that
243 ARRD-6 may play a regulatory role in TMC-1 channel function or it may be involved in endocytosis of the
244 TMC-1 complex by recruitment of cytoskeleton proteins, akin to the role that α -arrestin plays in GPCR
245 regulation^{40,41}. At this juncture we do not know why we observed only a single ARRD-6 subunit bound to
246 the complex, as there is sufficient space for two. Perhaps one subunit unbound from the complex or the
247 second subunit is only partially occupied. Further experiments are required to address these questions.

248 **Mapping the putative ion channel pore**

249 Single-channel currents measured from cochlear hair cells demonstrate that the mammalian MT
250 complex is cation-selective with a high permeability for Ca^{2+} ⁴². TMC-1, or TMC-2, are likely the pore-
251 forming subunits of the mammalian MT complex and cysteine mutagenesis experiments have pinpointed
252 several pore-lining residues critical for TMC-1-mediated MT^{7,8}. While *C. elegans* TMC-1 mediates
253 mechanosensitivity in worm OLQ neurons and body wall muscles¹³, its ion selectivity and permeation
254 properties are not known, largely due to challenges associated with heterologous expression of the
255 recombinant complex and with vanishingly small amounts of native material. Interestingly, *C. elegans* and
256 murine TMC-1 also function as Na^+ permeable leak channels that modulate the resting membrane potential
257 via a depolarizing background leak conductance, suggesting that TMC-1 may serve multiple cellular roles
258^{23,43} and indicating that the channel pore is permeable to a greater diversity of ions than previously
259 appreciated.

260 To gain insight into the nature and function of the *C. elegans* TMC-1 ion conduction pathway, we
261 superimposed the TMC-1 subunit onto the structures of TMEM16A and OSCA1.2, revealing a similar
262 architecture among the transmembrane domains (Extended Data Fig. 6). The TMEM16A and OSCA1.2
263 dimer assemblies harbor two pores, one within each subunit, that are defined by helices TM3-TM7.

264 Structural similarities between TMEM16a and OSCA1.2 suggest that TMC-1 may also have two pores and
265 could conduct ions through a structurally analogous pathway composed of TM4-TM8 (Fig. 5a). The
266 putative ion conduction pathway appears closed, with a narrow pore blocked by three constrictions (Fig.
267 5b, c). Polar and basic residues line the first constriction site near the extracellular pore entrance and
268 nonpolar residues dominate the second constriction site, located ~ 20 Å farther 'down' the conduction
269 pathway, towards the cytoplasm. The remaining 40 Å of the conduction pathway is lined by mostly polar
270 and charged residues (Fig. 5d). Seven basic residues line the pore, two of which (H404 and H731) partially
271 define the third and narrowest constriction site. We visualized two spherical, non-protein densities near two
272 acidic residues (D683 and D695) that may correspond to bound cations (Fig. 5b). At the present resolution,
273 however, we cannot determine if these features are Ca^{2+} ions. Both Asp residues are conserved in human
274 TMC-1, suggesting that they are important for ion coordination. While the ionizable residues lining the
275 pore are predominately basic and thus not in keeping with a canonical Ca^{2+} -permeable channel, which is
276 typically dominated by acidic residues, the overall residue composition is similar to the mechanosensitive
277 ion channel OSCA1.2²⁹. OSCA1.2 displays stretch-activated non-selective cation currents with 17-21%
278 Cl^- permeability⁴⁴, suggesting *C. elegans* TMC-1 may exhibit similar permeation properties.

279 To visualize the ion conduction pore of the vertebrate MT complex, we exploited the *C. elegans*
280 structure and constructed a homology model of the human TMC-1 complex that includes TMC-1, CIB2
281 and TMIE (Supplementary Fig. 3). Upon inspection of the human structure, we found that the putative pore
282 is lined by two basic residues and five acidic residues, in keeping with the channel being permeable to Ca^{2+} .
283 In addition, there are relatively more polar residues compared to the worm ortholog and the histidine
284 residues that occlude the second constriction site in *C. elegans* TMC-1 are replaced by M418 and A579 in
285 the human model. The vertebrate MT complex also endows hair cells with permeability to organic
286 molecules, including the dye FM1-43^{45,46}. While our structure does not provide direct insight into the
287 pathway of small molecule permeation, several hydrophobic crevices, including the lipid-lined space
288 between TMC-1 and TMIE, provide possible routes for the transmembrane passage of small molecules
289 such as FM1-43.

290 **‘Expanded’ and ‘Contracted’ conformations**

291 We discovered a second conformation of the TMC-1 complex via 3D classification, termed the ‘C’
292 conformation (Fig. 6a). The TMC-1 subunits in the ‘E’ and ‘C’ conformations have a similar structure and
293 both have closed ion channels. In the ‘C’ conformation, however, the TM10 helix is bent $\sim 9^\circ$ compared
294 with that of ‘E’, and we can observe one more helical turn of TM10 in the ‘E’ conformation. Upon
295 successively superimposing the TMC-1 subunits from the ‘C’ and ‘E’ complexes we observe that in the ‘E’
296 state, each half of the TMC-1 complex, composed of TMC-1/CALM-1/TMIE subunits, are rotated by $\sim 8^\circ$
297 in comparison to the ‘C’ state, by way of an axis of rotation that is located near the TMC-1 H7-H8 helices
298 and oriented approximately parallel to the membrane. The movement of each half of the complex, when
299 viewed parallel to the membrane plane, thus resembles the motion of an accordion, with the cytoplasmic
300 regions of the complex undergoing relatively larger conformational displacements in comparison to those
301 on the extracellular side of the membrane. Indeed, in comparing the ‘C’ and ‘E’ states, the amphipathic
302 TMC-1 H3 helices move farther apart by $\sim 11 \text{ \AA}$, thus underscoring the magnitude of the conformational
303 change. Together, these results illustrate the conformational plasticity of the TMC-1 complex and,
304 reciprocally, the possibility that deformations of the membrane may induce conformational changes in the
305 TMC-1 complex.

306 **Membrane embedding of the TMC-1 complex**

307 To understand how the TMC-1 complex interacts with individual lipids as well as with the lipid
308 bilayer, we performed all-atom (AA) and coarse-grained (CG) MD simulations on the complex embedded
309 in a membrane composed of phospholipids and cholesterol (Extended Data Fig. 9a). The AA set included
310 three independent simulation replicas yielding a collective sampling time of $3 \mu\text{s}$, whereas the CG
311 simulations were performed for $8 \mu\text{s}$ on a system including 4 TMC-1 complexes in a larger membrane patch
312 resulting in a sampling time of $32 \mu\text{s}$ of lipid-protein interactions (Extended Data Fig. 9a). The equilibrated
313 structure of the membrane around the TMC-1 complex indicates an unusually deep penetration and
314 anchoring of the amphipathic, ‘paddle’ H3 helix into the cytosolic leaflet of the bilayer (Fig. 6c). In
315 agreement with the cryo-EM density maps, the simulations show that phospholipids and cholesterol occupy

316 the cavity between TMIE and TMC-1 and cholesterol is enriched in crevices near the 2-fold related, TM10
317 helices at the TMC-1 subunit interface, together supporting the importance of lipids in the structure and
318 function of the complex (Extended Data Fig. 9b, c). The TMC-1 complex also distorts the membrane bilayer,
319 promoting both thinning and thickening of the membrane, with especially prominent thinning of the
320 cytoplasmic leaflet within the region of H3 helix insertion (Fig. 6d and Extended Data Fig. 9d). Strikingly,
321 the effect of the TMC-1 complex on the membrane bilayer is long-range and propagates up to ~ 50 Å from
322 the protein (Extended Data Fig. 9d), thus suggesting an interplay between membrane structure and the
323 function of the TMC-1 complex.

324 **Summary**

325 The molecular structures of the TMC-1 complex reveal the identity, architecture, and membrane
326 association of key subunits central to vertebrate and *C. elegans* mechanosensory transduction. The
327 accordion-shaped, 2-fold symmetric complex harbors TMIE subunits poised like ‘handles’ perpendicular
328 to the membrane, and amphipathic TMC-1 H3 helices inserted and parallel to the membrane plane, each
329 providing possible mechanisms for direct or indirect transduction of force to ion channel gating,
330 respectively. In vertebrates, protocadherin-15 transduces force to stereocilia tips, opening the MT channel.
331 Prior studies suggest that protocadherin-15 forms a stable, dimeric complex with LHFPL5 yet also interacts
332 with TMC-1 and TMIE subunits^{9,15,17,47,48}. How might protocadherin-15, either alone or in complex with
333 LHFPL5, interact with the TMC-1 complex? One possibility is that the protocadherin-15 dimer is situated
334 coincident with the 2-fold axis of the TMC-1 complex, with protocadherin-15 TMs ‘surrounding’ the TMC-
335 1 TM10 helices. This ‘closed’ symmetric dimeric complex would enable tension on protocadherin-15 to be
336 directly transduced to the TMC-1 complex via the protocadherin-15 contacts with the TM10 helices.
337 Alternatively, protocadherin-15 dimers could interact with TMIE helices, with one protocadherin subunit
338 interacting with a single TMIE subunit, thus forming an ‘open’ complex in which the ‘unpaired’
339 protocadherin-15 subunit could interact with a TMIE subunit from another TMC-1 complex. This model
340 not only provides a direct mechanism of force transduction from protocadherin-15 to TMIE and then to the

341 TMC-1 ion channel pore, but it also provides a mechanism for the clustering of TMC-1 complexes⁴⁹. In
 342 additional to direct transduction of force, we also speculate that H3 of the TMC-1 subunit acts like a paddle
 343 in the membrane that will move ‘up’ or ‘down’ as the membrane thins or thickens, thus providing a
 344 mechanism for force coupling to the channel via the membrane. Further studies of open-channel
 345 conformations of the *C. elegans* TMC-1 complex, in addition to structures of the vertebrate MT complex,
 346 will be required to more fully elucidate the mechanisms of force transduction. Nevertheless, these TMC-1
 347 complexes provide a framework for structure-based mechanisms of touch in *C. elegans* and of hearing and
 348 balance in vertebrates.

349 Main References

- 350 1 Musiek, F. E. & Baran, J. A. *The auditory system : anatomy, physiology, and clinical correlates*.
 351 Second edition. edn, (Plural Publishing, Inc., 2020).
- 352 2 Farhadi, M., Razmara, E., Balali, M., Hajabbas Farshchi, Y. & Falah, M. How Transmembrane
 353 Inner Ear (TMIE) plays role in the auditory system: A mystery to us. *J Cell Mol Med*,
 354 doi:10.1111/jcmm.16610 (2021).
- 355 3 Zheng, W. & Holt, J. R. The Mechanosensory Transduction Machinery in Inner Ear Hair Cells.
 356 *Annu Rev Biophys* **50**, 31-51, doi:10.1146/annurev-biophys-062420-081842 (2021).
- 357 4 Kazmierczak, P. *et al.* Cadherin 23 and protocadherin 15 interact to form tip-link filaments in
 358 sensory hair cells. *Nature* **449**, 87-91, doi:10.1038/nature06091 (2007).
- 359 5 Sakaguchi, H., Tokita, J., Muller, U. & Kachar, B. Tip links in hair cells: molecular composition
 360 and role in hearing loss. *Curr Opin Otolaryngol Head Neck Surg* **17**, 388-393,
 361 doi:10.1097/MOO.0b013e3283303472 (2009).
- 362 6 Kurima, K. *et al.* Dominant and recessive deafness caused by mutations of a novel gene, TMC1,
 363 required for cochlear hair-cell function. *Nat Genet* **30**, 277-284, doi:10.1038/ng842 (2002).
- 364 7 Pan, B. *et al.* TMC1 and TMC2 are components of the mechanotransduction channel in hair cells
 365 of the mammalian inner ear. *Neuron* **79**, 504-515, doi:10.1016/j.neuron.2013.06.019 (2013).
- 366 8 Pan, B. *et al.* TMC1 Forms the Pore of Mechanosensory Transduction Channels in Vertebrate Inner
 367 Ear Hair Cells. *Neuron* **99**, 736-753 e736, doi:10.1016/j.neuron.2018.07.033 (2018).
- 368 9 Zhao, B. *et al.* TMIE is an essential component of the mechanotransduction machinery of cochlear
 369 hair cells. *Neuron* **84**, 954-967, doi:10.1016/j.neuron.2014.10.041 (2014).
- 370 10 Pacentine, I. V. & Nicolson, T. Subunits of the mechano-electrical transduction channel, Tmc1/2b,
 371 require Tmie to localize in zebrafish sensory hair cells. *PLoS Genet* **15**, e1007635,
 372 doi:10.1371/journal.pgen.1007635 (2019).
- 373 11 Cunningham, C. L. *et al.* TMIE Defines Pore and Gating Properties of the Mechanotransduction
 374 Channel of Mammalian Cochlear Hair Cells. *Neuron* **107**, 126-143 e128,
 375 doi:10.1016/j.neuron.2020.03.033 (2020).
- 376 12 Giese, A. P. J. *et al.* CIB2 interacts with TMC1 and TMC2 and is essential for mechanotransduction
 377 in auditory hair cells. *Nature communications* **8**, 43, doi:10.1038/s41467-017-00061-1 (2017).
- 378 13 Tang, Y. Q. *et al.* Ankyrin Is An Intracellular Tether for TMC Mechanotransduction Channels.
 379 *Neuron* **107**, 112-125 e110, doi:10.1016/j.neuron.2020.03.026 (2020).

- 380 14 Liang, X. *et al.* CIB2 and CIB3 are auxiliary subunits of the mechanotransduction channel of hair
381 cells. *Neuron* **109**, 2131-2149 e2115, doi:10.1016/j.neuron.2021.05.007 (2021).
- 382 15 Xiong, W. *et al.* TMHS is an integral component of the mechanotransduction machinery of cochlear
383 hair cells. *Cell* **151**, 1283-1295, doi:10.1016/j.cell.2012.10.041 (2012).
- 384 16 Beurg, M., Xiong, W., Zhao, B., Muller, U. & Fettiplace, R. Subunit determination of the
385 conductance of hair-cell mechanotransducer channels. *Proceedings of the National Academy of
386 Sciences of the United States of America* **112**, 1589-1594, doi:10.1073/pnas.1420906112 (2015).
- 387 17 Ge, J. *et al.* Structure of mouse protocadherin 15 of the stereocilia tip link in complex with LHFPL5.
388 *Elife* doi: **10.7554/eLife.38770**. (2018).
- 389 18 Erickson, T. *et al.* Integration of Tmc1/2 into the mechanotransduction complex in zebrafish hair
390 cells is regulated by Transmembrane O-methyltransferase (Tomt). *Elife* **6**, doi:10.7554/eLife.28474
391 (2017).
- 392 19 Cunningham, C. L. *et al.* The murine catecholamine methyltransferase mTOMT is essential for
393 mechanotransduction by cochlear hair cells. *Elife* **6**, doi:10.7554/eLife.24318 (2017).
- 394 20 Effertz, T., Scharr, A. L. & Ricci, A. J. The how and why of identifying the hair cell mechano-
395 electrical transduction channel. *Pflugers Arch* **467**, 73-84, doi:10.1007/s00424-014-1606-z (2015).
- 396 21 Palczewski, K. G protein-coupled receptor rhodopsin. *Annu Rev Biochem* **75**, 743-767,
397 doi:10.1146/annurev.biochem.75.103004.142743 (2006).
- 398 22 Kawate, T. & Gouaux, E. Fluorescence-detection size-exclusion chromatography for
399 precrystallization screening of integral membrane proteins. *Structure* **14**, 673-681,
400 doi:10.1016/j.str.2006.01.013 (2006).
- 401 23 Yue, X. *et al.* TMC Proteins Modulate Egg Laying and Membrane Excitability through a
402 Background Leak Conductance in *C. elegans*. *Neuron* **97**, 571-585 e575,
403 doi:10.1016/j.neuron.2017.12.041 (2018).
- 404 24 Jain, A. *et al.* Probing cellular protein complexes using single-molecule pull-down. *Nature* **473**,
405 484-488, doi:10.1038/nature10016 (2011).
- 406 25 Michel, V. *et al.* CIB2, defective in isolated deafness, is key for auditory hair cell
407 mechanotransduction and survival. *EMBO Mol Med* **9**, 1711-1731,
408 doi:10.15252/emmm.201708087 (2017).
- 409 26 Brunner, J. D., Lim, N. K., Schenck, S., Duerst, A. & Dutzler, R. X-ray structure of a calcium-
410 activated TMEM16 lipid scramblase. *Nature* **516**, 207-212, doi:10.1038/nature13984 (2014).
- 411 27 Dang, S. *et al.* Cryo-EM structures of the TMEM16A calcium-activated chloride channel. *Nature*
412 **552**, 426-429, doi:10.1038/nature25024 (2017).
- 413 28 Paulino, C., Kalienkova, V., Lam, A. K. M., Neldner, Y. & Dutzler, R. Activation mechanism of
414 the calcium-activated chloride channel TMEM16A revealed by cryo-EM. *Nature* **552**, 421-425,
415 doi:10.1038/nature24652 (2017).
- 416 29 Jojoa-Cruz, S. *et al.* Cryo-EM structure of the mechanically activated ion channel OSCA1.2. *Elife*
417 **7**, doi:10.7554/eLife.41845 (2018).
- 418 30 Zhang, M. *et al.* Structure of the mechanosensitive OSCA channels. *Nat Struct Mol Biol* **25**, 850-
419 858, doi:10.1038/s41594-018-0117-6 (2018).
- 420 31 Kefauver, J. M., Ward, A. B. & Patapoutian, A. Discoveries in structure and physiology of
421 mechanically activated ion channels. *Nature* **587**, 567-576, doi:10.1038/s41586-020-2933-1 (2020).
- 422 32 Mitchem, K. L. *et al.* Mutation of the novel gene Tmie results in sensory cell defects in the inner
423 ear of spinner, a mouse model of human hearing loss DFNB6. *Hum Mol Genet* **11**, 1887-1898,
424 doi:10.1093/hmg/11.16.1887 (2002).
- 425 33 Shen, Y. C. *et al.* The transmembrane inner ear (tmie) gene contributes to vestibular and lateral line
426 development and function in the zebrafish (*Danio rerio*). *Dev Dyn* **237**, 941-952,
427 doi:10.1002/dvdy.21486 (2008).
- 428 34 Gleason, M. R. *et al.* The transmembrane inner ear (Tmie) protein is essential for normal hearing
429 and balance in the zebrafish. *Proceedings of the National Academy of Sciences of the United States
430 of America* **106**, 21347-21352, doi:10.1073/pnas.0911632106 (2009).

- 431 35 Sirmaci, A. *et al.* A founder TMIE mutation is a frequent cause of hearing loss in southeastern
432 Anatolia. *Clin Genet* **75**, 562-567, doi:10.1111/j.1399-0004.2009.01183.x (2009).
- 433 36 Riazuddin, S. *et al.* Alterations of the CIB2 calcium- and integrin-binding protein cause Usher
434 syndrome type 1J and nonsyndromic deafness DFNB48. *Nat Genet* **44**, 1265-1271,
435 doi:10.1038/ng.2426 (2012).
- 436 37 Wang, Y. *et al.* Loss of CIB2 Causes Profound Hearing Loss and Abolishes Mechanoelectrical
437 Transduction in Mice. *Front Mol Neurosci* **10**, 401, doi:10.3389/fnmol.2017.00401 (2017).
- 438 38 Lally, C. C., Bauer, B., Selent, J. & Sommer, M. E. C-edge loops of arrestin function as a membrane
439 anchor. *Nature communications* **8**, 14258, doi:10.1038/ncomms14258 (2017).
- 440 39 Xie, Y. *et al.* GPS-Lipid: a robust tool for the prediction of multiple lipid modification sites. *Sci*
441 *Rep* **6**, 28249, doi:10.1038/srep28249 (2016).
- 442 40 Becuwe, M. & Leon, S. Integrated control of transporter endocytosis and recycling by the arrestin-
443 related protein Rod1 and the ubiquitin ligase Rsp5. *Elife* **3**, doi:10.7554/eLife.03307 (2014).
- 444 41 Han, S. O., Kommaddi, R. P. & Shenoy, S. K. Distinct roles for beta-arrestin2 and arrestin-domain-
445 containing proteins in beta2 adrenergic receptor trafficking. *EMBO Rep* **14**, 164-171,
446 doi:10.1038/embor.2012.187 (2013).
- 447 42 Fettiplace, R. & Kim, K. X. The physiology of mechanoelectrical transduction channels in hearing.
448 *Physiol. Rev.* **94**, 951-986 (2014).
- 449 43 Liu, S. *et al.* TMC1 is an essential component of a leak channel that modulates tonotopy and
450 excitability of auditory hair cells in mice. *Elife* **8**, doi:10.7554/eLife.47441 (2019).
- 451 44 Murthy, S. E. *et al.* OSCA/TMEM63 are an Evolutionarily Conserved Family of Mechanically
452 Activated Ion Channels. *Elife* **7**, doi:10.7554/eLife.41844 (2018).
- 453 45 Gale, J. E., Marcotti, W., Kennedy, H. J., Kros, C. J. & Richardson, G. P. FM1-43 dye behaves as
454 a permeant blocker of the hair-cell mechanotransducer channel. *The Journal of neuroscience : the*
455 *official journal of the Society for Neuroscience* **21**, 7013-7025 (2001).
- 456 46 Meyers, J. R. *et al.* Lighting up the senses: FM1-43 loading of sensory cells through nonselective
457 ion channels. *The Journal of neuroscience : the official journal of the Society for Neuroscience* **23**,
458 4054-4065 (2003).
- 459 47 Maeda, R. *et al.* Tip-link protein protocadherin 15 interacts with transmembrane channel-like
460 proteins TMC1 and TMC2. *Proceedings of the National Academy of Sciences of the United States*
461 *of America* **111**, 12907-12912, doi:10.1073/pnas.1402152111 (2014).
- 462 48 Maeda, R., Pacentine, I. V., Erickson, T. & Nicolson, T. Functional Analysis of the Transmembrane
463 and Cytoplasmic Domains of Pcdh15a in Zebrafish Hair Cells. *The Journal of neuroscience : the*
464 *official journal of the Society for Neuroscience* **37**, 3231-3245, doi:10.1523/JNEUROSCI.2216-
465 16.2017 (2017).
- 466 49 Beurg, M. *et al.* Variable number of TMC1-dependent mechanotransducer channels underlie
467 tonotopic conductance gradients in the cochlea. *Nature communications* **9**, 2185,
468 doi:10.1038/s41467-018-04589-8 (2018).
- 469

471 **Materials and Methods**

472 **Transgenic worm design.** The strain PHX2173 *tmc-1(syb2173)* was generated by SunyBiotech using
473 CRISPR/Cas9 genome editing and is referred to as the *tmc-1::mVenus* line (Supplementary Fig. 1). The
474 TMC-1-mVenus-3xFLAG sequence was inserted prior to the stop codon of the endogenous *tmc-1* gene
475 (Wormbase: T13G4.3.1). The genotype was confirmed using PCR and primers ER02-seq-s
476 (ATTAGATCCCGCAAGAGAAT) and ER02-seq-a (AAGGTGATATGAACGAACCG), which bind
477 452bp upstream and 408 bp downstream from the insertion site, respectively to amplify the region of
478 interest. The PCR product was subsequently sequenced using primers ER02-mid-s
479 (CATGAAGCAACACGACTTCT) and ER02-mid-a (TCTTCGATGTTGTGACGGAT), which bind
480 within the TMC-1-mVenus-3xFLAG sequence. To enable elution of the engineered TMC-1 complex from
481 affinity chromatography resin, a PreScission protease (3C) cleavage site was placed between the C-terminus
482 of TMC-1 and the mVenus fluorophore.

483 **Spectral confocal imaging.** Adult worms were immobilized in M9 buffer (22 mM KH₂PO₄, 42
484 mM Na₂HPO₄, 86 mM NaCl, and 1 mM MgCl₂) containing 30 mM sodium azide and placed on slides that
485 were prepared with ~4 mm agar pads. Spectral images were acquired on a Zeiss 34-channel LSM 880 Fast
486 Airyscan inverted microscope with a 40x 1.2 NA water-immersion objective lens. Linear unmixing was
487 employed to distinguish between the mVenus signal and autofluorescence. The autofluorescence signal was
488 subtracted from each image. The 3D z-stack information is presented in 2D after performing a maximum
489 intensity projection.

490 **Large scale *C. elegans* culture.** All *C. elegans* strains were maintained and grown according to
491 Wormbook methods (<http://www.wormbook.org>). For large scale liquid culture, nematode growth medium
492 (NGM) agar plates were prepared and spread with *E. coli* strain HB101, allowing the bacterial lawn to grow
493 overnight at 37 °C. Worms were transferred to the NGM plates and grown for 3-4 days at 20 °C until HB101
494 cells were depleted. Worms on the plates were transferred to a liquid medium in 2L baffled flasks,
495 supplemented with HB101 (~15g per 500 mL medium) and streptomycin (50 µg/mL), and worms were

496 grown at 20 °C with vigorous shaking (150 rpm) for 70-72 hours. To harvest worms, the liquid culture
497 flasks were placed on ice for 1 hour to allow the worms to settle. The media was removed, and the worm
498 slurry was collected in a tube, washed twice with 50 mL of ice cold M9 buffer by successive centrifugation
499 (800 x g for 1 minute) and resuspension. Worms were 'cleaned' by sucrose density centrifugation at 1500
500 x g for 5 minutes after bringing the volume of worm slurry up to 25 mL with M9 buffer and adding 25 mL
501 of ice cold 60% (w/v) sucrose. The worm layer on top was recovered and placed in a new tube and then
502 washed twice with 50 mL of ice cold M9 buffer. The volume of the worm pellet was measured and the
503 same volume of M9 buffer was added to the tube and worm balls were made by dripping the slurry into
504 liquid nitrogen. The worm balls were stored at -80 °C until further use.

505 **Isolation of the native TMC-1 complex.** Approximately 80 g of frozen worm balls were disrupted
506 using a ball mill (MM400, Retch) where the grinding jar and ball were pre-cooled in liquid nitrogen.
507 Disrupted worm powder was solubilized at 4 °C for 2 hours in a buffer containing 50 mM Tris-Cl (pH 9.3),
508 50 mM NaCl, 5 mM EDTA, 2% (w/v) glyco-diosgenin (GDN), and protease inhibitors (0.8 μM aprotinin,
509 2 μg/mL leupeptin and 2 μM pepstatin). After centrifugation at 40,000 rpm (186,000 x g) for 50 minutes,
510 the supernatant was applied to anti-FLAG M2 affinity resin and incubated overnight on a rotator at 4°C.
511 The resin was washed 5 times with a buffer containing 20 mM Tris-Cl (pH 8.5), 150 mM NaCl and 0.02%
512 (w/v) GDN, using a volume of buffer that was 200-fold the volume of the resin. The TMC-1 complex was
513 eluted by incubating with 40 μg of 3C protease at 4 °C for 4 hours on the rotator. Subsequently, the solution
514 was supplemented with 3 mM CaCl₂, final concentration, and the eluate was filtered with a 0.22 μm
515 centrifuge tube filter. The concentrate was loaded onto a size-exclusion chromatography (SEC) column
516 (Superose 6 Increase 10/30 GL, GE Healthcare), equilibrated in a buffer composed of 20 mM Tris-Cl (pH
517 8.5), 150 mM NaCl, 0.02% (w/v) GDN and 3 mM CaCl₂. The peak fractions from the putative dimeric
518 TMC-1 complex were pooled and concentrated for cryo-EM grid preparation. Approximately 50 ng of
519 TMC-1 was isolated from 80 g of worm balls, which translates to approximately 6×10^7 worms. The amount
520 of protein was determined via mVenus fluorescence based on a standard plot. The estimated total amount

521 of the TMC-1 complex including TMC-1, CALM-1 and TMIE is 60 ng. The isolated native TMC-1 sample
522 was analyzed by SDS-PAGE (sodium dodecyl sulfate–polyacrylamide gel electrophoresis) and the protein
523 bands were visualized by silver staining. For mass-spectrometry analysis, the putative dimeric TMC-1
524 complex peak was pooled and concentrated to a volume of 50 μ L for further use. The same isolation method
525 was utilized to make the wild-type worm sample from the *C. elegans* N2 strain for use as a control in the
526 mass spectrometry experiments in order to evaluate non-specific binding of *C. elegans* proteins to anti-
527 FLAG M2 affinity resin.

528 **Isolation of the native TMC-1 complex for SiMPull.** The native TMC-1 complex, bound to anti-
529 FLAG M2 affinity resin, was eluted via a buffer composed of 20 mM Tris-Cl (pH 8.5), 150 mM NaCl and
530 0.02% (w/v) GDN, supplemented with 1 mg/mL 2X FLAG peptide at 4 °C for 40 minutes on a rotator. The
531 eluate was concentrated and subjected to further purification on a SEC column. The putative dimeric TMC-
532 1 complex peak was pooled and used for SiMPull.

533 **SiMPull.** Coverslips and glass slides were cleaned, passivated and coated with a solution consisting
534 of 50 mM methoxy polyethylene glycol (mPEG) and 1.25 mM biotinylated PEG in water. A flow chamber
535 was created by drilling 0.75 mm holes in a quartz slide and by placing double-sided tape between the holes.
536 A coverslip was placed on top of the slide and the edges were sealed with epoxy, creating small flow
537 chambers. A solution of phosphate buffered saline (PBS) that included 0.25 mg/mL streptavidin was then
538 applied to the slide, allowed to incubate for 5 minutes, and washed off with a buffer consisting of 50 mM
539 Tris, 50 mM NaCl and 0.25 mg/mL bovine serum albumin (BSA), pH 8.0 (T50 BSA buffer). Biotinylated
540 anti-GFP nanobody in T50 BSA at 10 μ g/mL was applied to the slide, allowed to incubate for 10 minutes,
541 and washed off with 30 μ L buffer A (20 mM Tris, pH 8.0, 150 mM NaCl, 0.02% (w/v) GDN, 3 mM CaCl_2).

542 The TMC-1 complex was isolated as previously described under ‘isolation of the native TMC-1
543 complex for SiMPull’. The complex was purified by SEC, diluted 1:200, and immediately applied to the
544 chamber. After a 5-minute incubation, the slide was washed with 30 μ L buffer A and the chamber was
545 imaged using a Leica DMi8 TIRF microscope with an oil-immersion 100x objective. Images were captured

546 using a back-illuminated EMCCD camera (Andor iXon Ultra 888) with a $133 \times 133 \mu\text{m}$ imaging area and
547 a $13 \mu\text{m}$ pixel size. This $13 \mu\text{m}$ pixel size corresponds to 130 nm on the sample due to the 100x objective.
548 To estimate non-specific binding to the glass slide, the purified TMC-1 complex was applied to a separate
549 chamber wherein the anti-GFP nanobody was not included and the other steps remained identical. The
550 observed spot count from this chamber was used to estimate the number of background fluorescence spots.

551 Photobleaching movies were acquired by exposing the imaging area for 60 seconds. To count the
552 number of TMC-1 subunits, single-molecule fluorescence time traces of the mVenus-tagged TMC-1
553 complex were generated using a custom python script. Each trace was manually scored as having one to
554 three bleaching steps or was discarded if no clean bleaching steps could be identified. The resulting
555 distribution of bleaching steps closely matches a binomial distribution for a dimeric protein based on an
556 estimated GFP maturation of 80%. A total of 600 molecules were evaluated from three separate movies.
557 Scoring was verified by assessing the intensity of the spot; on average, the molecules that bleach in 2 steps
558 were twice as bright as those that bleach in 1 step.

559 **Mass spectrometry.** The purified TMC-1 complex sample was dried, dissolved in 5% sodium
560 dodecyl sulfate, 8 M urea, 100 mM glycine (pH 7.55), reduced with (tris(2-carboxyethyl)phosphine (TCEP)
561 at 37°C for 15 min, alkylated with methyl methanethiosulfonate for 15 min at room temperature followed
562 by addition of acidified 90% methanol and 100 mM triethylammonium bicarbonate buffer (TEAB; pH 7.55).
563 The sample was then digested in an S-trap micro column briefly with $2 \mu\text{g}$ of a Tryp/LysC protease mixture,
564 followed by a wash and 2 hr digestion at 47°C with trypsin. The peptides were eluted with 50 mM TEAB
565 and 50% acetonitrile, 0.2% formic acid, pooled and dried. Each sample was dissolved in $20 \mu\text{L}$ of 5%
566 formic acid and injected into Thermo Fisher QExactive HF mass spectrometer. Protein digests were
567 separated using liquid chromatography with a Dionex RSLC UHPLC system, then delivered to a QExactive
568 HF (Thermo Fisher) using electrospray ionization with a Nano Flex Ion Spray Source (Thermo Fisher)
569 fitted with a $20 \mu\text{m}$ stainless steel nano-bore emitter spray tip and 1.0 kV source voltage. Xcalibur version
570 4.0 was used to control the system. Samples were applied at $10 \mu\text{L}/\text{min}$ to a Symmetry C18 trap cartridge

571 (Waters) for 10 min, then switched onto a 75 μm x 250 mm NanoAcquity BEH 130 C18 column with 1.7
572 μm particles (Waters) using mobile phases water (A) and acetonitrile (B) containing 0.1% formic acid, 7.5-
573 30% acetonitrile gradient over 60 min and 300 nL/min flow rate. Survey mass spectra were acquired over
574 m/z 375-1400 at 120,000 resolution (m/z 200) and data-dependent acquisition selected the top 10 most
575 abundant precursor ions for tandem mass spectrometry by higher energy collisional dissociation using an
576 isolation width of 1.2 m/z, normalized collision energy of 30 and a resolution of 30,000. Dynamic exclusion
577 was set to auto, charge state for MS/MS +2 to +7, maximum ion time 100 ms, minimum AGC target of 3
578 $\times 10^6$ in MS1 mode and 5×10^3 in MS2 mode. Data analysis was performed using Comet (v. 2016.01, rev.
579 3)⁵⁰ against a January 2022 version of canonical FASTA protein database containing *C. elegans* uniprot
580 sequences and concatenated sequence-reversed entries to estimate error thresholds and 179 common
581 contaminant sequences and their reversed forms. Comet searches for all samples performed with trypsin
582 enzyme specificity with monoisotopic parent ion mass tolerance set to 1.25 Da and monoisotopic fragment
583 ion mass tolerance set at 1.0005 Da. A static modification of +45.9877 Da was added to all cysteine residues
584 and a variable modification of +15.9949 Da on methionine residues. A linear discriminant transformation
585 was used to improve the identification sensitivity from the Comet analysis^{51,52}. Separate histograms were
586 created for matches to forward sequences and for matches to reversed sequences for all peptides of seven
587 amino acids or longer. The score histograms of reversed matches were used to estimate peptide false
588 discovery rates (FDR) and set score thresholds for each peptide class. The overall protein FDR was 1.2%.

589 **Cryo-EM sample preparation.** A volume of 3.5 μL of the concentrated TMC-1 complex was
590 applied to a Quantifoil grid (R2/1 300 gold mesh, covered by 2 nm continuous carbon film), which was
591 glow-discharged at 15 mA for 30 seconds in the presence of amylamine. The grids were blotted and flash
592 frozen using a Vitrobot mark IV for 2.5 seconds with 0 blot force after 30 seconds wait time under 100%
593 humidity at 15 $^{\circ}\text{C}$. The grids were plunge-frozen into liquid ethane, cooled by liquid nitrogen.

594 **Data acquisition.** The native TMC-1 complex dataset was collected on a 300 keV FEI Titan Krios
595 microscope equipped with a K3 detector. The micrographs were acquired in super-resolution mode (0.4195

596 Å/pixel) with a magnification of 105kx corresponding to a physical pixel size of 0.839 Å/pixel. Images
597 were collected by a 3×3 multi-hole per stage shift and a 6 multi-shot per hole method using Serial EM, with
598 a defocus range of −1.0 to −2.4 μm. Each movie stack was exposed for 3.3 seconds and consisted of 50
599 frames per movie, with a total dose of 50 e⁻/Å². A total of 26,055 movies were collected.

600 **Image processing.** Beam-induced motion was corrected by patch motion correction with an output
601 Fourier cropping factor of 1/2 (0.839 Å/pixel). Contrast transfer function (CTF) parameters were estimated
602 by patch CTF estimation in CryoSparc v3.3.1⁵³. A total of 25,852 movies were selected by manual curation
603 and the particles were picked by using blob-picker with minimum and maximum particle diameters of 140
604 Å and 200 Å, respectively. Initially, 7.9 million particles were picked and extracted with a box size of 400
605 pixels and binned 4x (3.356 Å/pixel). After one round of 2D classification, ‘junk’ particles were removed,
606 resulting in 3.2 million particles in total. The particles with the highest resolution features, approximately
607 1.5 million, were used for *ab initio* reconstruction. The full particle stack consisting of 3.2 million particles
608 from 2D classification were then subjected to heterogeneous refinement using the reconstructed models
609 from the *ab initio* reconstruction. Probable monomeric TMC-1 complexes, detergent micelles, and
610 additional junk particles were removed in this step, yielding 1.65 million particles. Particles were then re-
611 extracted from unbinned images. Subsequently, heterogeneous refinement using C1 symmetry was
612 performed with the re-extracted 1.65 million particles, yielding 8 classes. Among them, three good classes
613 composed of 667k particles were selected and used for further analysis. After one round of heterogeneous
614 refinement with 4 classes in C2 symmetry, two classes containing 208k and 199k particles were discerned,
615 each with distinct features and that we describe as the ‘contracted’ and ‘expanded’ forms, respectively. One
616 more round of heterogeneous refinement was performed for both particle stacks to sort out groups of
617 homogeneous particles from each class. To attain higher resolution and improved map quality, non-uniform
618 refinement including defocus and global CTF refinement was performed in Cryosparc v3.3.1 of each
619 individual class, with particle stack sizes of 141k (contracted) and 142k (expanded), resulting in resolutions
620 at 3.09 Å and 3.10 Å, respectively.

621 Among the initial 8 classes from the heterogeneous refinement of 1.65 million particles, one of the
622 classes, which contained 272k particles, had an additional density feature, proximal to CALM-1. Further
623 heterogeneous refinement and 3D classification without alignment was carried out with this class to sort
624 out heterogeneous particles. One more round of heterogeneous refinement in Cryosparc resulted in one
625 promising particle class, containing 99k particles, out of four total classes. Non uniform refinement,
626 including defocus and global CTF refinement, was performed with the selected class, resulting in a map at
627 3.54 Å resolution. To improve the density of unknown protein bound to CALM-1, local refinement in
628 Cryosparc was performed using a mask, covering the ‘extra density’ and CALM-1.

629 **Structure determination and model building.** The initial EM density map was sharpened with
630 Phenix AutoSharpen⁵⁴, and both sharpened and unsharpened maps were used for structure determination.
631 Various strategies including *de novo* building, structure prediction, docking and homologous modeling
632 were used for model building. The transmembrane helices of TMC-1 (TM1–TM9, excluding TM10),
633 predicted by Alphafold2⁵⁵ as a template, were fit into the map with rigid body fitting in UCSF Chimera⁵⁶
634 and *de novo* model building using Coot⁵⁷. The possible ion permeation pore of the channel was determined
635 by MOLE 2.0⁵⁸. Carbohydrate groups were modeled to protruding densities of N209 on TMC-1, at a
636 predicted *N*-linked glycosylation site.

637 To build the structure of CALM-1 into the ‘expanded’ conformation density map of the TMC-1
638 complex, we exploited the previously determined structure of CIB3 in complex with a TMC-1 peptide
639 (PDB 6WUD). We docked CIB3 into the density map using rigid body fitting in UCSF Chimera, using the
640 highly conserved H5-H6 helices of TMC-1 as a guidepost, and proceeded by introducing the sequence of
641 CALM-1 into the model, followed by manual adjustment of the model using Coot. Conserved bulky side
642 chains, including F84, Y129, and F197, that protrude into hydrophobic cavities and are facing the helices
643 of TMC-1, facilitated the definition of the correct register of the CALM-1 sequence.

644 The auxiliary subunit, TMIE, was built manually into the density map of the ‘expanded’
645 conformation using Coot. The bulky side chain density of tryptophan (W25) and lipid modification on

646 cysteine residue (C44) helped to assign the sequence register in the context of the density map. The model
647 was refined against the sharpened map by real-space refinement in Phenix.

648 The following regions of TMC-1 were not modeled into the map because of weak or absent
649 densities: The N-terminal region of TMC-1 (M1 to P73), the predicted loop region between TM5 and TM6
650 (S460 to N663) and the C-terminal region (L886 to D1285). The side chains with weak density on H1 (75-
651 87) and TM10 (870-885) helices were modeled as alanine residues. The N-terminal region of CALM-1,
652 from residues 1 to 17, and the amino acids of TMIE, including 1-17 and 64-117, were not modeled due to
653 a lack of density. As discussed in the main text, we suggest that residues 1-17 of TMIE comprise a signal
654 peptide.

655 For the modeling of the unknown density on CALM-1 we speculated that ARRD-6 was a possible
656 candidate auxiliary protein based on the mass spectrometry results. Although the overall map quality of the
657 putative ARRD-6 region was not sufficient for *de novo* model building, we could find several β -sheets with
658 side chain densities on the map. Using the predicted structure of ARRD-6 and the crossed-protrusion of
659 two loops of the N- and C- domains of arrestin (82-85 of the N-, and 249-256 of the C- domain), we could
660 align the predicted ARRD-6 model into the unknown density, thus providing further evidence that the
661 unknown density is ARRD-6. The estimated local resolution of ARRD-6 density ranges between 4-7 Å and
662 the calculated Q-score of ARRD-6 model-to-map from MapQ⁵⁹ plugin in Chimera is 0.25, which
663 corresponds to the estimated resolution of 4.91 Å, suggesting that the model is reasonably placed in the
664 map. The final CC of the ARRD-6 and overall model are 0.42 and 0.69, respectively.

665 **Molecular Dynamics Simulations**

666 The molecular dynamics (MD) simulations were performed on the 'E' conformation and at two
667 different resolutions, coarse-grained (CG) and all-atom (AA). Starting from the cryo-EM modeled structure,
668 a C-terminal carboxylic cap group, an N-terminal ammonium capping group, missing side chains and all
669 the hydrogen atoms were modeled using the PSFGEN plugin of VMD⁶⁰. PROPKA was employed to

670 estimate the pKa of titratable residues^{61,62}. The modeled structure was then used for setting up the CG and
671 AA simulations.

672 **Coarse-grained simulation setup.** The Martini-based CG model⁶³⁻⁶⁵ of the 'E' conformation was
673 generated, employing the Martinize protocol as described in the Martini website (<http://www.cgmartini.nl/>),
674 followed by applying an elastic network on atom pairs within a 10 Å cut-off. The CG parameters for the
675 palmitoylated Cys in TMIE was obtained from a previous work⁶⁶. The initial orientation of the protein in
676 the membrane was adopted from the Orientations of Proteins in Membranes (OPM) database. The protein
677 complex was then inserted in a lipid bilayer composed of palmitoyl-oleoyl-phosphatidyl-ethanolamine (PE),
678 palmitoyl-oleoyl-phosphatidyl-choline (PC), sphingomyelin (SM), and cholesterol with a molar ratio of
679 54:32:8:6. The secondary structure of the protein was derived from the AA model and maintained
680 throughout the CG simulations. To enhance the sampling and improve statistics, four copies of the protein
681 were embedded in a large patch ($400 \times 400 \text{ \AA}^2$) of lipid bilayer at an inter-protein distance of 200 Å, using
682 the computer program 'insane'⁶⁷. The system was then solvated and ionized with 150 mM NaCl
683 concentration employing insane (system size: 330k CG beads).

684 **All-atom simulation setup.** The CG equilibrated protein-membrane complex at the end of the 8
685 μs CG simulation was back-mapped to a CHARMM-based AA model employing CHARMM-GUI^{68,69}.
686 Thus, one of the four replicas (a protein copy with membrane padding of approximately 40 Å) was isolated
687 from the large membrane patch. DOWSER was used to internally hydrate the protein^{70,71}. The protein-
688 membrane system was then solvated with water including 150 mM NaCl in VMD (system size: 340k atoms).
689 To improve the statics and further reduce any bias from the initial lipid placement, three independent
690 membrane systems, with independently placed initial lipids, were generated using the Membrane Mixer
691 Plugin (MMP)⁷².

692 **Coarse-grained simulation protocol.** CG systems were simulated using GROMACS⁷³, with the
693 standard Martini v2.2 simulation parameters⁶⁵. The simulation was conducted with a 20 fs timestep. The
694 temperature was fixed at 310 K using velocity-rescaling thermostat⁷⁴ with a time constant for coupling of

695 1 ps. A semi-isotropic 1-bar pressure was maintained employing the Berendsen barostat⁷⁵ with a
696 compressibility of 3×10^{-4} bar and a relaxation time constant of 5 ps. The system was initially energy
697 minimized for 1000 steps, followed by relaxation runs of 18 ns, while the lipid bilayer headgroups and
698 protein backbones were restrained harmonically. During the initial 18 ns, the restraints applied on bilayer
699 headgroups were removed stepwise (from $k = 200 \text{ kJ.mol}^{-1}.\text{nm}^{-2}$ to zero), while the restraints on protein
700 backbone ($k = 1000 \text{ kJ.mol}^{-1}.\text{nm}^{-2}$) were unchanged. The four-protein system was then simulated for 8 μs ,
701 with restraints only applied to the protein backbones, resulting in a cumulative sampling of 32 μs (4 copies
702 $\times 8 \mu\text{s}$).

703 **All-atom simulation protocol.** The AA converted system was simulated using the following
704 protocol: (1) 5,000 steps of minimization, followed by 5 ns of relaxation, during which the proteins' heavy
705 atoms as well as the bound Ca^{2+} ions were harmonically restrained ($k = 10 \text{ kcal.mol}^{-1}.\text{\AA}^{-2}$) to their position
706 in the cryo-EM model; (2) 1 ns of equilibration with harmonic restraints only on the protein backbone heavy
707 atoms ($k = 10 \text{ kcal.mol}^{-1}.\text{\AA}^{-2}$). The coordination of Ca^{2+} ions in this step was maintained by the application
708 of the Extra Bonds algorithm in NAMD^{76,77}. (3) 200 ps of equilibration during which the restraints on the
709 backbone were maintained whereas the Extra Bonds on the Ca^{2+} ions were removed. (4) Two additional
710 replicas were generated employing the MMP plugin and 1 μs of production run was performed on each of
711 the three replicas while only the protein backbone heavy atoms were restrained. Steps 1-3 were performed
712 using NAMD2^{76,77}. The 1- μs production runs for all three replicas were conducted on Anton2⁷⁸.

713 All AA simulations were performed using the fully atomistic CHARMM36m⁷⁹ and CHARMM36
714⁸⁰ force fields for the protein and lipids, respectively. Water molecules were modeled with TIP3P⁸¹. In
715 NAMD simulations, a 12 \AA cutoff was used for short-range, non-bonded interactions, with switching
716 distance starting at 10 \AA . Particle mesh Ewald (PME) was used to calculate long-range electrostatic
717 interactions⁸² with a grid density of 1 \AA^{-1} , and a PME interpolation order of 6. The SHAKE algorithm was
718 used to constrain bonds involving hydrogen atoms⁸³. Temperature was kept constant at 310 K using
719 Langevin thermostat with a damping coefficient of 1.0 ps^{-1} . Pressure was maintained at 1 atm employing

720 the Nosé-Hoover Langevin piston barostat with period and decay of 100 and 50 fs, respectively^{84,85}. All
 721 systems were simulated in a flexible cell allowing the dimensions of the periodic cell to change
 722 independently while keeping the aspect ratio in the xy plane (membrane plane) constant. The timestep was
 723 set to 2 fs, and the PME and Lennard-Jones forces were updated at every other and each timesteps,
 724 respectively.

725 For Anton2 simulations, 310 K temperature and 1 bar pressure were kept by the Nosé-Hoover
 726 chain coupling and Martyna-Tuckerman-Klein schemes⁸⁴, as implemented using a multigrator scheme⁸⁶.
 727 M-SHAKE was used to constrain all the bonds to hydrogen atoms⁸⁷, and a 2.5 fs timestep was used in all
 728 the simulations. The long-range electrostatic interactions were calculated by employing the Fast Fourier
 729 Transform (FFT) method on Anton2⁷⁸.

730 **Membrane thickness and lipid distribution analysis.** The change in the thickness of each
 731 membrane leaflet in response to the protein was quantified in both CG and AA simulations by monitoring
 732 the z (membrane normal) distance of the phosphate groups of phospholipids with respect to the bilayer
 733 midplane, over the second half of each trajectory (last 4 μ s of the CG simulations and the last 500 ns of the
 734 AA simulations). The thickness values were plotted using a histogram with $2 \times 2 \text{ \AA}^2$ bins in the xy plane
 735 (membrane plane), for each leaflet individually. Cholesterol and phospholipid distributions were similarly
 736 calculated by histogramming the positions of the hydroxy (for cholesterol) and phosphate (for
 737 phospholipids) beads over the last 4 μ s of the trajectory.

738 **Lipid depletion/enrichment analysis.** First, individual lipid counts for all lipid species within 7 \AA
 739 (using cholesterol or phospholipid phosphate beads) of the 4 protein copies over the 8 μ s of the CG
 740 simulation were determined. A depletion/enrichment index for lipid type L was then defined using the
 741 following equation⁸⁸:

$$742 \quad \text{Depletion/Enrichment index (L)} = \frac{\text{Ratio(L)}_{7\text{\AA}}}{\text{Ratio(L)}_{\text{bulk}}}$$

743 where:

744
$$Ratio(L)_{7\text{\AA}} = \frac{\text{Number of lipid type L within } 7\text{\AA} \text{ of protein copies}}{\text{Total number of lipids within } 7\text{\AA} \text{ of protein copies}}$$

745
$$Ratio(L)_{\text{bulk}} = \frac{\text{Number of lipid type L in the membrane}}{\text{Total number of lipids in the membrane}}$$

746 **Homology modeling of human TMC-1 complex.** The cryo-EM structure of the ‘E’ conformation
747 of *C. elegans* TMC-1 complex (containing 6 different chains: 2 TMC-1, 2 CALM-1 and 2 TMIE) was used
748 as a template to build a homology model of human TMC-1 complex. Each chain in the template structure
749 was isolated and its sequence was aligned to the corresponding human sequence with AlignMe⁸⁹. The
750 aligned sequences were then used in the multi-chain capability of MODELLER⁹⁰ to generate a human
751 TMC-1 complex. The discrete optimized protein energy (DOPE)⁹¹ and GA341^{92,93} methods were used to
752 assess the quality of the generated model. The optimization was performed with a maximum iteration of
753 300 and the model with the best molecular probability density function (molpdf) was selected (Extended
754 Data Fig. 9). The entire optimization cycle was repeated twice to obtain a better structure.

755

756 **Data Availability**

757 The coordinates and volumes for the cryo-EM data have been deposited in the Electron Microscopy
758 Data Bank under accession codes EMD-26741 (Expanded), EMD-26742 (Contracted), and EMD-26743
759 (with ARRD-6). The coordinates have been deposited in the Protein Data Bank under accession codes
760 7USW (Expanded), 7USX (Contracted), and 7USY (with ARRD-6).

761

762 **Acknowledgements**

763 We thank T. Nicolson, P. Barr-Gillespie, D. Farrens, M. Mayer, A. Aballay, Gouaux and Bacongus lab
764 members for helpful discussions, T. Provitola for assistance with figures, A. Reddy for mass spectrometric
765 analysis, J. Meyers and S. Yang for help with cryo-EM screening and data collection, and R. Hallford for
766 proof reading. Initial cryo-EM grids were screened at the Pacific Northwest Cryo-EM Center (PNCC),

767 which is supported by NIH grant U24GM129547 and performed at the PNCC at OHSU, accessed through
768 EMSL (grid.436923.9), a DOE Office of Science User Facility sponsored by the Office of Biological and
769 Environmental Research. The large single particle cryo-EM data set was collected at the Janelia Research
770 Campus of the Howard Hughes Medical Institute (HHMI). The OHSU Proteomics Shared Resource is
771 partially supported by NIH core grants P30EY010572 and P30CA069533. This work was supported by
772 NIH grant 1F32DC017894 to S.C. E.G. is an investigator of the HHMI. The simulations were supported
773 by the NIH grants, P41-GM104601 and R01-GM123455 to E.T. Simulations were performed using
774 allocations on Anton at Pittsburgh Supercomputing Center (award MCB100017P to E.T.), and XSEDE
775 resources provided by the National Science Foundation Supercomputing Centers (XSEDE grant number
776 MCA06N060 to E.T.).

777

778 **Author Contributions**

779 H.J., S.C., and A.G. performed the experiments. H.J., S.C., and A.G., together with E.G., designed the
780 project and wrote the manuscript. S.D.-G., A.R., and E.T. performed and analyzed MD simulations. All
781 authors contributed to manuscript preparation.

782

783 **Competing Interests**

784 The authors declare no competing interests.

785

786 **Additional Information**

787 Supplementary Information is available for this paper.

788

789 **Materials and Correspondence**

790 Correspondence and requests for materials should be addressed to E.G. Reprints and permissions
791 information is available at www.nature.com/reprints.

792 **Methods References**

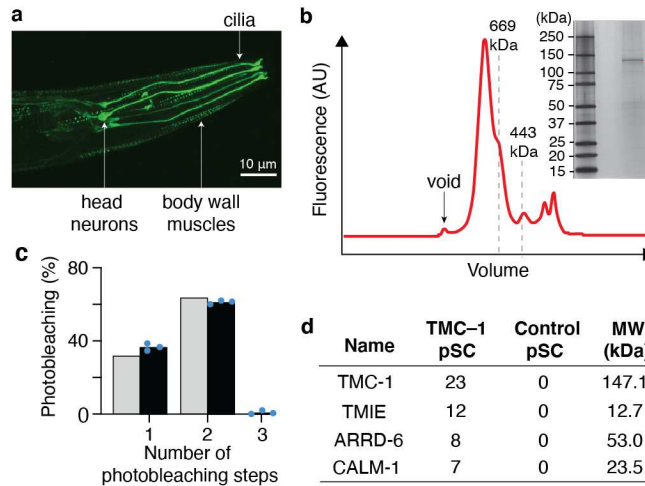
- 793
794 50 Eng, J. K., Jahan, T. A. & Hoopmann, M. R. Comet: an open-source MS/MS sequence database
795 search tool. *Proteomics* **13**, 22-24, doi:10.1002/pmic.201200439 (2013).
- 796 51 Wilmarth, P. A., Riviere, M. A. & David, L. L. Techniques for accurate protein identification in
797 shotgun proteomic studies of human, mouse, bovine, and chicken lenses. *J Ocul Biol Dis Infor* **2**,
798 223-234, doi:10.1007/s12177-009-9042-6 (2009).
- 799 52 Keller, A., Nesvizhskii, A. I., Kolker, E. & Aebersold, R. Empirical statistical model to estimate
800 the accuracy of peptide identifications made by MS/MS and database search. *Anal Chem* **74**, 5383-
801 5392, doi:10.1021/ac025747h (2002).
- 802 53 Punjani, A., Rubinstein, J. L., Fleet, D. J. & Brubaker, M. A. cryoSPARC: algorithms for rapid
803 unsupervised cryo-EM structure determination. *Nat. Methods* **14**, 290-296 (2017).
- 804 54 Adams, P. D. *et al.* PHENIX: building new software for automated crystallographic structure
805 determination. *Acta Crystallogr. D. Biol. Crystallogr.* **58**, 1948-1954 (2002).
- 806 55 Jumper, J. *et al.* Highly accurate protein structure prediction with AlphaFold. *Nature* **596**, 583-589,
807 doi:10.1038/s41586-021-03819-2 (2021).
- 808 56 Pettersen, E. F. *et al.* UCSF Chimera--a visualization system for exploratory research and analysis.
809 *J. Comput. Chem.* **25**, 1605-1612 (2004).
- 810 57 Emsley, P., Lohkamp, B., Scott, W. G. & Cowtan, K. Features and development of Coot. *Acta*
811 *Crystallogr. D. Biol. Crystallogr.* **66**, 486-501 (2010).
- 812 58 Sehnal, D. *et al.* MOLE 2.0: advanced approach for analysis of biomacromolecular channels. *J*
813 *Cheminform* **5**, 39, doi:10.1186/1758-2946-5-39 (2013).
- 814 59 Pintilie, G. *et al.* Measurement of atom resolvability in cryo-EM maps with Q-scores. *Nature*
815 *methods* **17**, 328-334, doi:10.1038/s41592-020-0731-1 (2020).
- 816 60 Humphrey, W., Dalke, A. & Schulten, K. VMD: visual molecular dynamics. *J Mol Graph* **14**, 33-
817 38, 27-38, doi:10.1016/0263-7855(96)00018-5 (1996).
- 818 61 Olsson, M. H., Sondergaard, C. R., Rostkowski, M. & Jensen, J. H. PROPKA3: Consistent
819 Treatment of Internal and Surface Residues in Empirical pKa Predictions. *J Chem Theory Comput*
820 **7**, 525-537, doi:10.1021/ct100578z (2011).
- 821 62 Sondergaard, C. R., Olsson, M. H., Rostkowski, M. & Jensen, J. H. Improved Treatment of Ligands
822 and Coupling Effects in Empirical Calculation and Rationalization of pKa Values. *J Chem Theory*
823 *Comput* **7**, 2284-2295, doi:10.1021/ct200133y (2011).
- 824 63 Periole, X. & Marrink, S. J. The Martini coarse-grained force field. *Methods in molecular biology*
825 *(Clifton, N.J.)* **924**, 533-565, doi:10.1007/978-1-62703-017-5_20 (2013).
- 826 64 Monticelli, L. *et al.* The MARTINI Coarse-Grained Force Field: Extension to Proteins. *J Chem*
827 *Theory Comput* **4**, 819-834, doi:10.1021/ct700324x (2008).
- 828 65 de Jong, D. H. *et al.* Improved Parameters for the Martini Coarse-Grained Protein Force Field. *J*
829 *Chem Theory Comput* **9**, 687-697, doi:10.1021/ct300646g (2013).
- 830 66 Atsmon-Raz, Y. & Tieleman, D. P. Parameterization of Palmitoylated Cysteine, Farnesylated
831 Cysteine, Geranylgeranylated Cysteine, and Myristoylated Glycine for the Martini Force Field. *J*
832 *Phys Chem B* **121**, 11132-11143, doi:10.1021/acs.jpcc.7b10175 (2017).
- 833 67 Wassenaar, T. A., Ingolfsson, H. I., Bockmann, R. A., Tieleman, D. P. & Marrink, S. J.
834 Computational Lipidomics with insane: A Versatile Tool for Generating Custom Membranes for
835 Molecular Simulations. *J Chem Theory Comput* **11**, 2144-2155, doi:10.1021/acs.jctc.5b00209
836 (2015).
- 837 68 Jo, S., Kim, T., Iyer, V. G. & Im, W. CHARMM-GUI: a web-based graphical user interface for
838 CHARMM. *J Comput Chem* **29**, 1859-1865, doi:10.1002/jcc.20945 (2008).
- 839 69 Wassenaar, T. A., Pluhackova, K., Bockmann, R. A., Marrink, S. J. & Tieleman, D. P. Going
840 Backward: A Flexible Geometric Approach to Reverse Transformation from Coarse Grained to
841 Atomistic Models. *J Chem Theory Comput* **10**, 676-690, doi:10.1021/ct400617g (2014).

- 842 70 Zhang, L. & Hermans, J. Hydrophilicity of cavities in proteins. *Proteins* **24**, 433-438,
843 doi:10.1002/(SICI)1097-0134(199604)24:4<433::AID-PROT3>3.0.CO;2-F (1996).
- 844 71 Gumbart, J., Trabuco, L. G., Schreiner, E., Villa, E. & Schulten, K. Regulation of the protein-
845 conducting channel by a bound ribosome. *Structure* **17**, 1453-1464, doi:10.1016/j.str.2009.09.010
846 (2009).
- 847 72 Licari, G., Dehghani-Ghahnaviyeh, S. & Tajkhorshid, E. Membrane Mixer: A Toolkit for Efficient
848 Shuffling of Lipids in Heterogeneous Biological Membranes. *J Chem Inf Model* **62**, 986-996,
849 doi:10.1021/acs.jcim.1c01388 (2022).
- 850 73 Hess, B., Kutzner, C., van der Spoel, D. & Lindahl, E. GROMACS 4: Algorithms for Highly
851 Efficient, Load-Balanced, and Scalable Molecular Simulation. *J Chem Theory Comput* **4**, 435-447,
852 doi:10.1021/ct700301q (2008).
- 853 74 Bussi, G., Donadio, D. & Parrinello, M. Canonical sampling through velocity rescaling. *J Chem*
854 *Phys* **126**, 014101, doi:10.1063/1.2408420 (2007).
- 855 75 Berendsen, H. J. C., Postma, J. P. M., van Gunsteren, W. F., DiNola, A. & Haak, J. R. Molecular
856 dynamics with coupling to an external bath. *J. Chem. Phys.* **81**, 1-2 (1984).
- 857 76 Phillips, J. C. *et al.* Scalable molecular dynamics on CPU and GPU architectures with NAMD. *J*
858 *Chem Phys* **153**, 044130, doi:10.1063/5.0014475 (2020).
- 859 77 Phillips, J. C. *et al.* Scalable molecular dynamics with NAMD. *J Comput Chem* **26**, 1781-1802,
860 doi:10.1002/jcc.20289 (2005).
- 861 78 Shaw, D. E. *et al.* in *SC '14: Proceedings of the International Conference for High Performance*
862 *Computing, Networking, Storage and Analysis.* (IEEE).
- 863 79 Huang, J. *et al.* CHARMM36m: an improved force field for folded and intrinsically disordered
864 proteins. *Nature methods* **14**, 71-73, doi:10.1038/nmeth.4067 (2017).
- 865 80 Klauda, J. B. *et al.* Update of the CHARMM all-atom additive force field for lipids: validation on
866 six lipid types. *J Phys Chem B* **114**, 7830-7843, doi:10.1021/jp101759q (2010).
- 867 81 Jorgensen, W. L., Chandrasekhar, J., Madura, J. D., Impey, R. W. & Klein, M. L. Comparison of
868 simple potential functions for simulation of liquid water *J. Chem. Phys.* **79**, 926-935 (1983).
- 869 82 Darden, T., York, D. & Pedersen, L. Particle mesh Ewald: An N.log(N) method for Ewald sums in
870 large systems. *J. Chem. Phys.* **98**, 10089-10092 (1993).
- 871 83 Ryckaert, J.-P., Ciccotti, G. & Berendsen, H. J. C. Numerical integration of the cartesian equations
872 of motion of a system with constraints: molecular dynamics of n-alkanes. *J. Comput. Physics* **23**,
873 327-341 (1977).
- 874 84 Martyna, G. J., Tobias, D. J. & Klein, M. L. Constant pressure molecular dynamics algorithms. *J.*
875 *Chem. Phys.* **101**, 4177-4189 (1994).
- 876 85 Feller, S. E., Zhang, Y. & Pastor, R. W. Constant pressure molecular dynamics simulations: The
877 Langevin piston method. *J. Chem. Phys.* **103**, 4613-4621 (1995).
- 878 86 Lippert, R. A. *et al.* Accurate and efficient integration for molecular dynamics simulations at
879 constraint temperature and pressure. *J. Chem. Phys.* **139**, 164106-164106 (2013).
- 880 87 Kräutler, V., van Gunsteren, W. F. & Hünenberger, P. H. A fast SHAKE algorithm to solve distance
881 constraint equations for small molecules in molecular dynamics simulations. *J. Comput. Chem.* **22**,
882 501-508 (2001).
- 883 88 Corradi, V. *et al.* Lipid-Protein Interactions Are Unique Fingerprints for Membrane Proteins. *ACS*
884 *Cent Sci* **4**, 709-717, doi:10.1021/acscentsci.8b00143 (2018).
- 885 89 Stamm, M., Staritzbichler, R., Khafizov, K. & Forrest, L. R. AlignMe--a membrane protein
886 sequence alignment web server. *Nucleic Acids Res* **42**, W246-251, doi:10.1093/nar/gku291 (2014).
- 887 90 Webb, B. & Sali, A. Protein Structure Modeling with MODELLER. *Methods in molecular biology*
888 *(Clifton, N.J.)* **2199**, 239-255, doi:10.1007/978-1-0716-0892-0_14 (2021).
- 889 91 Shen, M. Y. & Sali, A. Statistical potential for assessment and prediction of protein structures.
890 *Protein Sci* **15**, 2507-2524, doi:10.1110/ps.062416606 (2006).
- 891 92 Melo, F., Sanchez, R. & Sali, A. Statistical potentials for fold assessment. *Protein Sci* **11**, 430-448,
892 doi:10.1002/pro.110430 (2002).

893 93 John, B. & Sali, A. Comparative protein structure modeling by iterative alignment, model building
894 and model assessment. *Nucleic Acids Res* **31**, 3982-3992, doi:10.1093/nar/gkg460 (2003).

895

896

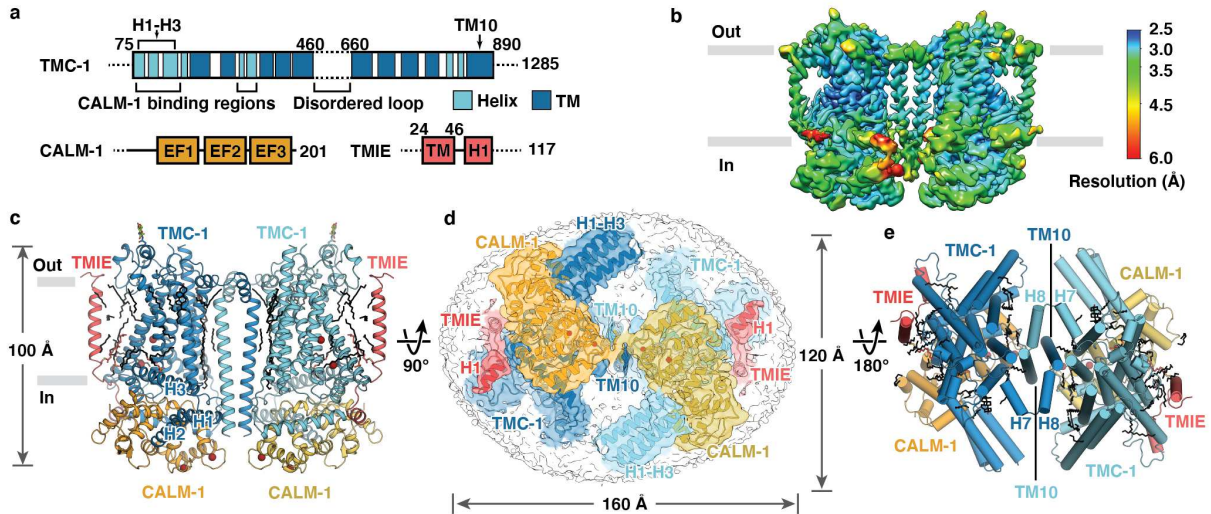


897

898 **Fig. 1. Dimeric TMC-1 complex from *C. elegans* copurifies with additional proteins.**

899 **a**, Spectral confocal image of mVenus fluorescence in an adult *tmc-1::mVenus* worm showing mVenus
 900 fluorescence in the head neurons, cilia and body wall muscles. Shown is one representative image of five
 901 total images. **b**, Representative FSEC profile of the TMC-1 complex, detected via the mVenus tag. Inset
 902 shows a silver-stained, SDS-PAGE gel of the purified TMC-1 complex. Red asterisk indicates TMC-1. **c**,
 903 The distribution of mVenus photobleaching steps for the TMC-1 complex is consistent with a binomial
 904 function (grey bars) an assembly with two fluorophores. A total of $n = 600$ spots were analyzed from three
 905 photobleaching movies (200 spots per movie). Each movie is represented by a blue dot. **d**, Analysis of
 906 TMC-1 complex by mass spectrometry (MS) shows selected identified proteins in order of decreasing
 907 peptide spectral counts. Proteins that were identified in the TMC-1 sample, but not in the control sample
 908 from wild-type worms, are shown. A full table can be found in Extended Data Fig. 2.

909

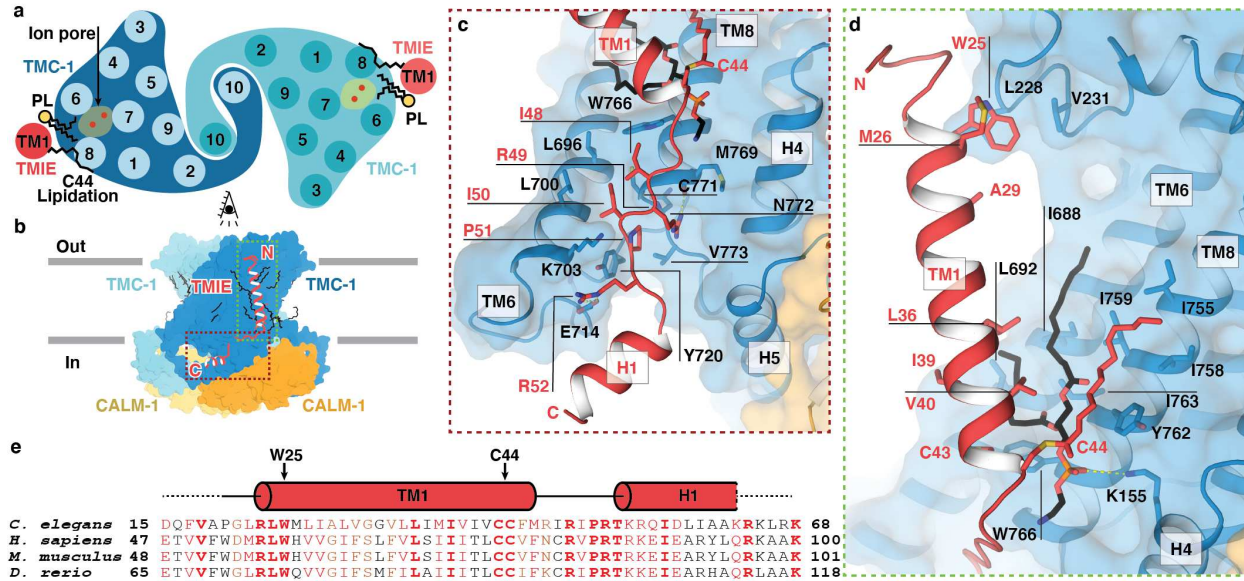


910

911 **Fig. 2. Architecture and subunit arrangement of the TMC-1 complex.**

912 **a**, Schematic representation of protein constructs that were isolated with TMC-1. **b**, Local resolution map
 913 of native TMC-1 complex after three-dimensional reconstruction. **c**, Overall architecture of native TMC-1
 914 complex, viewed parallel to the membrane. TMC-1 (dark blue and light blue), CALM-1 (orange and yellow)
 915 and TMIE (red and pink) are shown in a cartoon diagram. Lipid-like molecules, *N*-Glycans, and putative
 916 ions are colored black, green, and dark red, respectively. **d**, Cytosolic view of the reconstructed map, fitted
 917 with the model. Subunit densities are colored as same in c) and the detergent micelle is shown in grey. **e**, A
 918 top-down extracellular view of the TMC-1 complex shows the domain-swapped dimeric interface. α -
 919 helices are represented as cylinders.

920

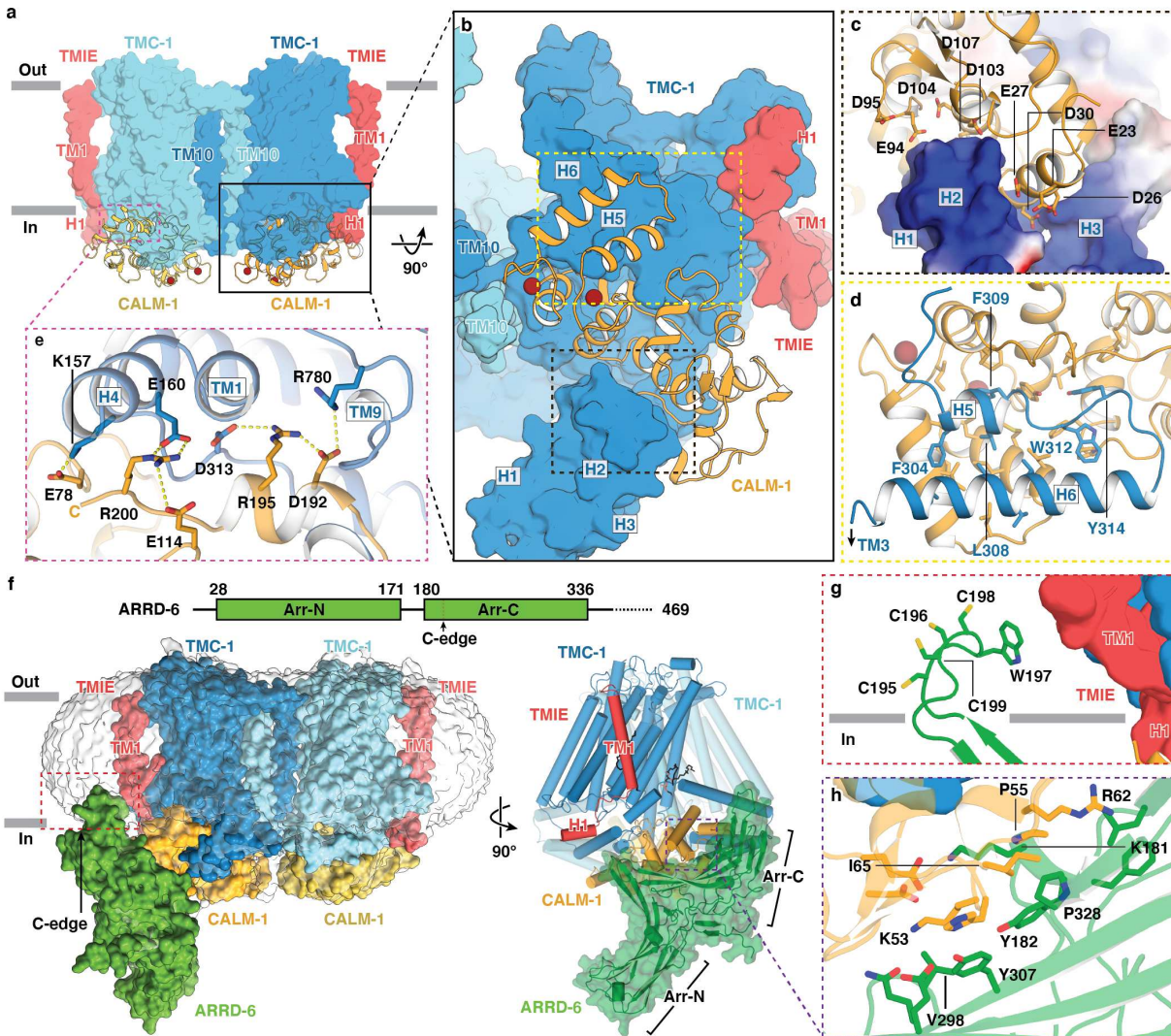


921

922 **Fig. 3. TMIE resides on the periphery of the TMC-1 complex.**

923 **a**, Schematic representation of TMC-1 (blue) and TMIE (red) transmembrane helices highlights the
 924 proximity of TMIE to the putative TMC-1 ion conduction pathway. Palmitoylation of TMIE C44 and
 925 phospholipids are shown in black. **b**, Overview of the interaction interface between TMIE and TMC-1,
 926 viewed from the side. **c**, Interface between the TMIE ‘elbow’ and TMC-1. Interacting residues are shown
 927 as sticks. **d**, Interface between TMIE transmembrane helix and TMC-1, highlighting key residues and lipids.
 928 Palmitoylation is shown in red and phospholipid is shown in black. **e**, Multiple sequence alignment of TMIE
 929 orthologs. Elements of secondary structure are shown above the sequences and key residues are indicated
 930 with black arrows.

931



932

933 **Fig. 4. CALM-1 and ARR-6 auxiliary subunits cap the cytoplasmic face of the TMC-1 complex.**

934 Binding interface between CALM-1 and TMC-1 viewed **a**, parallel to the membrane and **b**, perpendicular

935 to the membrane. **c**, Binding interface between CALM-1 and TMC-1 H1-H3. The electrostatic surface of

936 TMC-1 is shown, where blue represents basic regions and red represents acidic regions. CALM-1 is shown

937 in yellow. **d**, Interface between CALM-1 and TMC-1 H5-H6. **e**, Salt bridges between the C-terminus of

938 CALM-1 and TMC-1. Putative hydrogen bonds are shown as dashed lines. **f**, 3D reconstruction of the

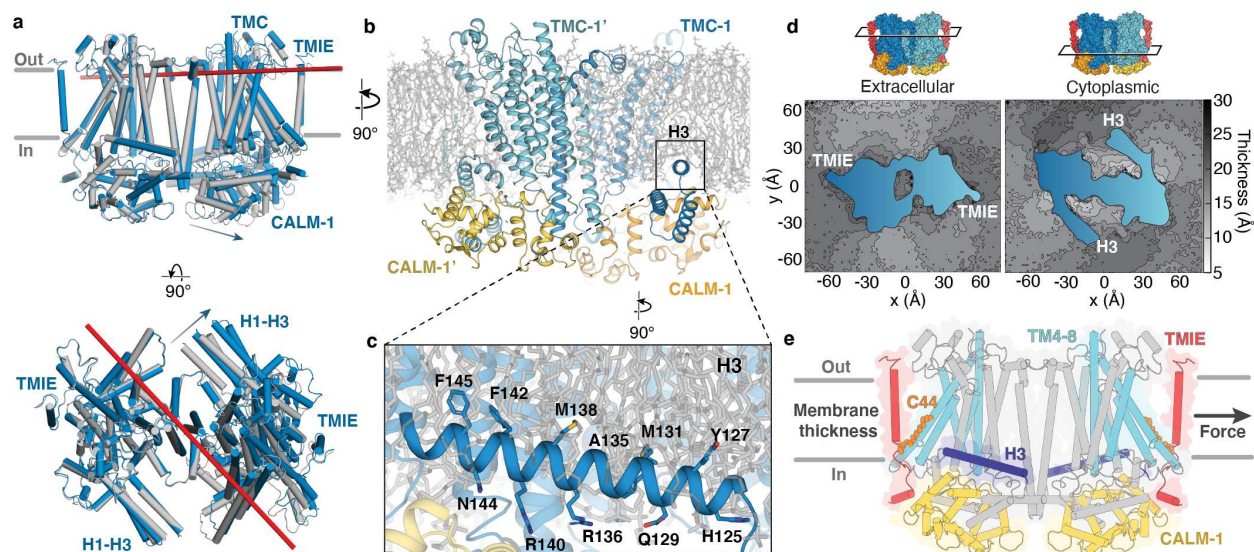
939 TMC-1 complex with ARR-6 viewed parallel to the membrane. TMC-1, CALM-1, TMIE, and ARR-6

940 are shown in blue, yellow, red, and green, respectively. A red dashed rectangle indicates the putative

941 insertion site of the ARR-6 C-edge loop into the micelle. A schematic diagram of ARR-6 is shown

942 above the reconstruction. **g**, Interface between the C-edge loop of ARRD-6 and the membrane. ARRD-6
943 residues that likely participate in membrane interactions are shown as sticks. **h**, Interface between ARRD-
944 6 (green) and CALM-1 (yellow), highlighting residues that are important for the binding interaction.

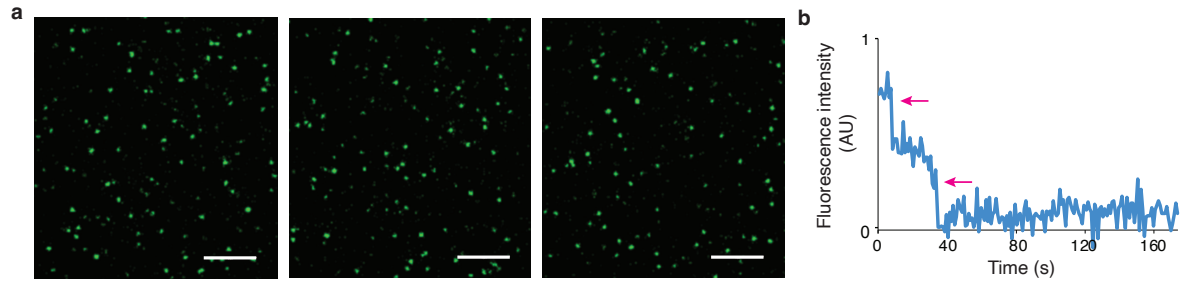
945



956

957 **Fig. 6. Conformational flexibility and membrane integration of the TMC-1 complex.**

958 **a**, A TMC-1 protomer from the ‘E’ conformation (blue) and the ‘C’ conformation (grey) were superposed
 959 based on backbone alpha-carbon atoms, revealing conformational differences in TMC-1, as well as CALM-
 960 1 and TMIE. The axis of rotation is shown as a red bar and arrows indicate the direction of rotation from
 961 the ‘C’ to the ‘E’ state. **b**, MD simulation of the membrane-embedded TMC-1 complex shows deep
 962 penetration of the H3 helix into the lipid bilayer. **c**, Key residues that define the amphipathic nature of the
 963 H3 helix are shown as sticks. **d**, Lipid bilayer thickness for extracellular and cytosolic leaflets averaged
 964 over the last 500 ns of all three simulated replicas. The cross-section of the protein is shown in blue and the
 965 location of the cross section is indicated above the plots using a surface representation of the TMC-1
 966 complex. Dark grey and light grey shades in the heatmaps represent membrane thinning and thickening,
 967 respectively. **e**, Schematic illustrating mechanisms by which direct or indirect forces are transduced to ion
 968 channel gating. TMIE is shown in red and palmitoylation of C44 is shown as orange spheres. The putative
 969 pore-forming helices of TMC-1 are shown in light blue, H3 is depicted in dark blue, and CALM-1 is yellow.
 970 Grey arrow (right) shows how membrane tension could directly gate the TMC-1 complex by exerting force
 971 on TMIE. Indirect force as a result of changes in membrane thickness could affect the position of the
 972 membrane embedded helix H3, modulating ion channel gating.



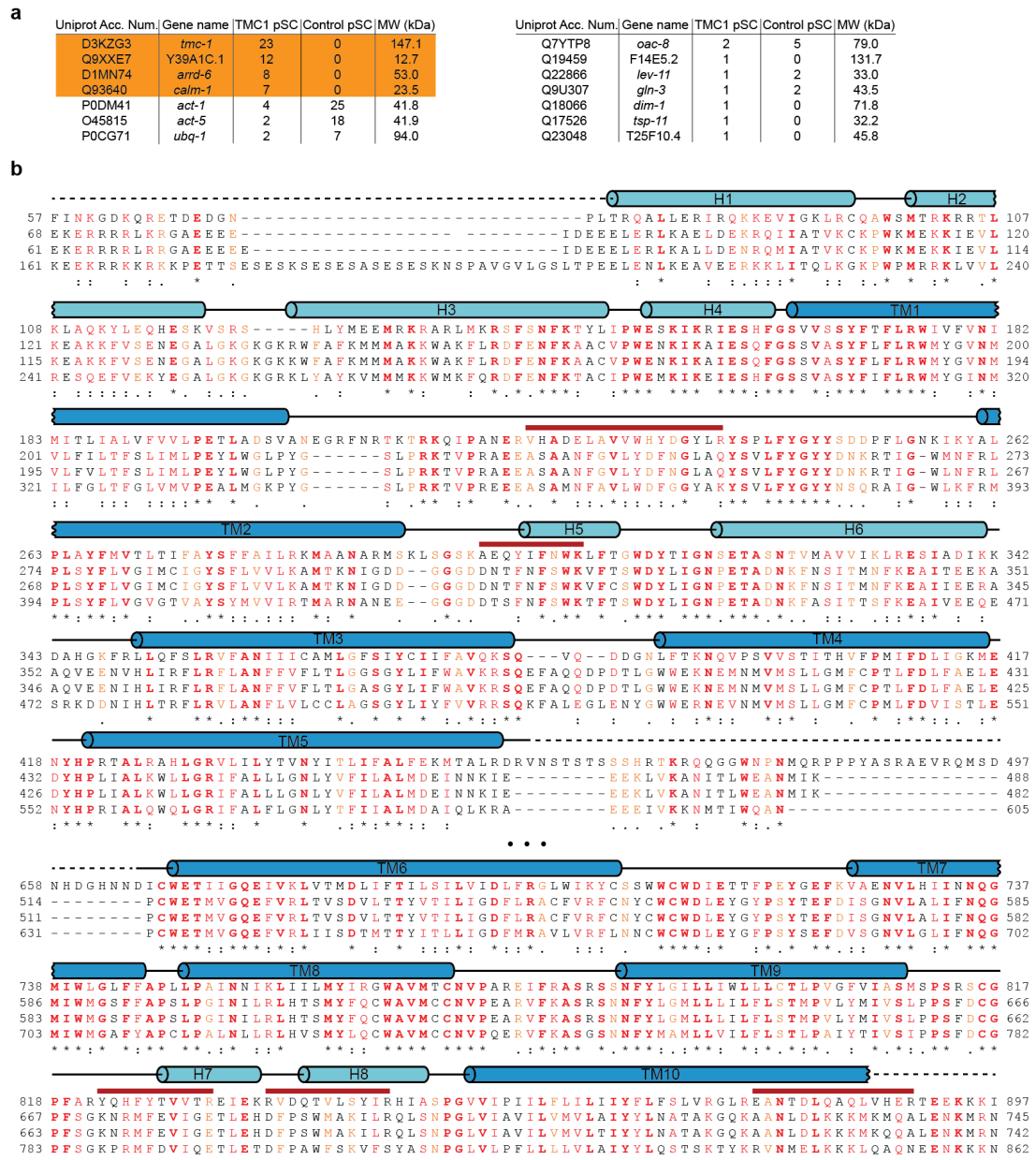
973

974 **Extended Data Fig. 1. Representative TIRF images and photobleaching traces for the native,**
975 **mVenus-tagged TMC-1 complex.**

976 **a**, Images are shown for the SEC-purified mVenus-tagged TMC-1 complex captured with biotinylated anti-
977 GFP nanobody. Scale bar = 5 μm . **b**, Representative trace showing the two-step photobleaching (red arrows)
978 of the mVenus-tagged TMC-1 complex.

979

980



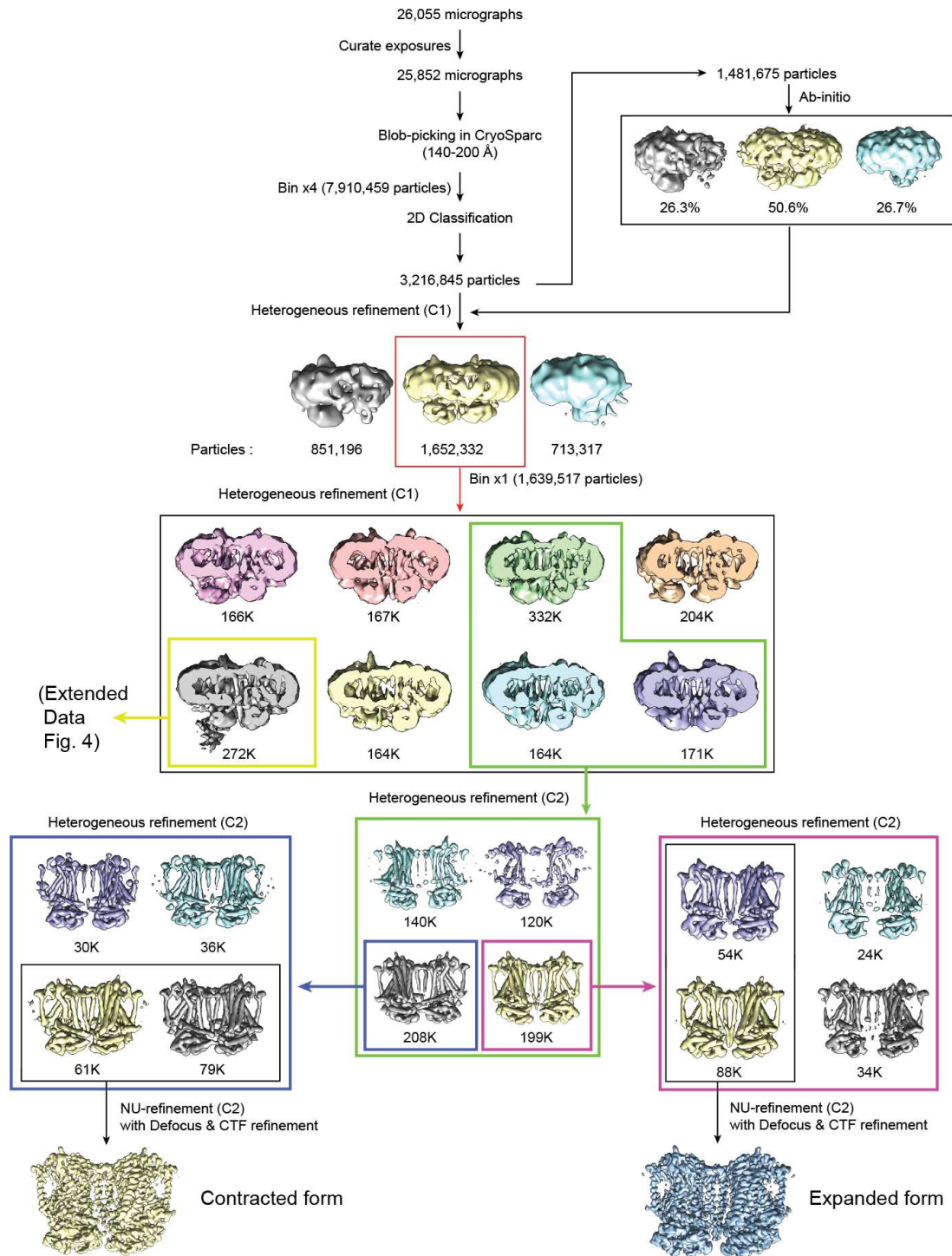
981

982 **Extended Data Fig. 2. MS analysis of the TMC-1 complex.**

983 **a**, Proteins detected by MS, via their associated peptide fragments, are listed with their gene name and
 984 molecular mass. The number of identified unique peptides from both the native TMC-1 complex and from
 985 wild-type worms (*C. elegans* N2), used as a control, are also indicated. **b**, Amino acid sequence and
 986 secondary structure of *C. elegans* TMC-1 are shown. The secondary structure based on the cryo-EM

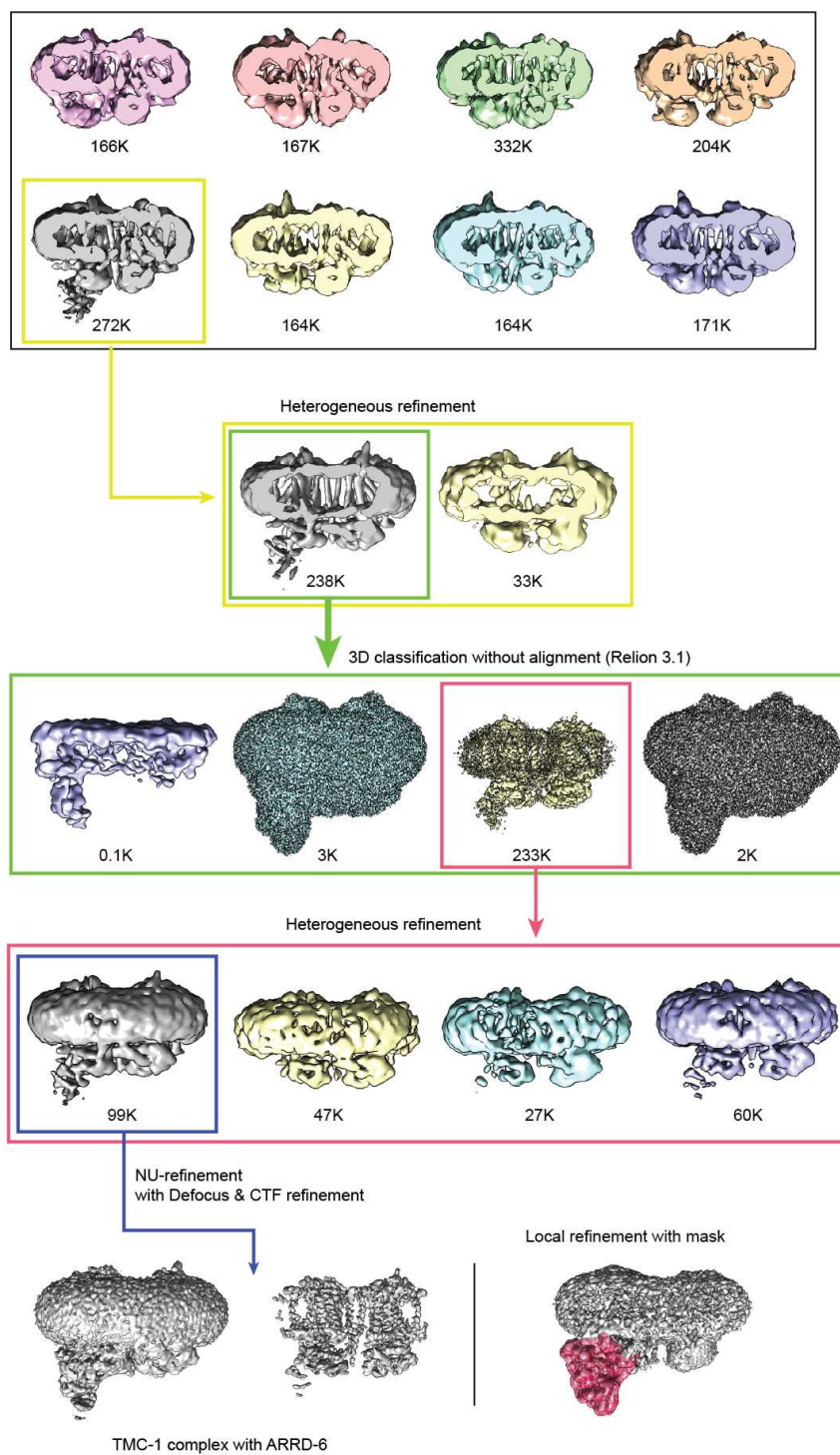
987 structure is indicated above the sequences as boxes (α -helices), black lines (loop regions), or dashed lines
988 (disordered residues). Peptides found by MS are indicated below the sequence (red lines). Note that the
989 TMC-1 segments, corresponding to the sequence of 13-33, 557-566, 567-587, 877-890, 897-904, 917-927,
990 972-996, 1041-1052, 1177-1190, 1192-1216, and 1261-1269 are also found by MS, but not indicated in **b**.
991
992

993



994 **Extended Data Fig. 3. Cryo-EM processing workflow of ‘E’ and ‘C’ conformations.**

995 Flow chart for cryo-EM data analysis of ‘E’ and ‘C’ conformation of the TMC-1 complex.

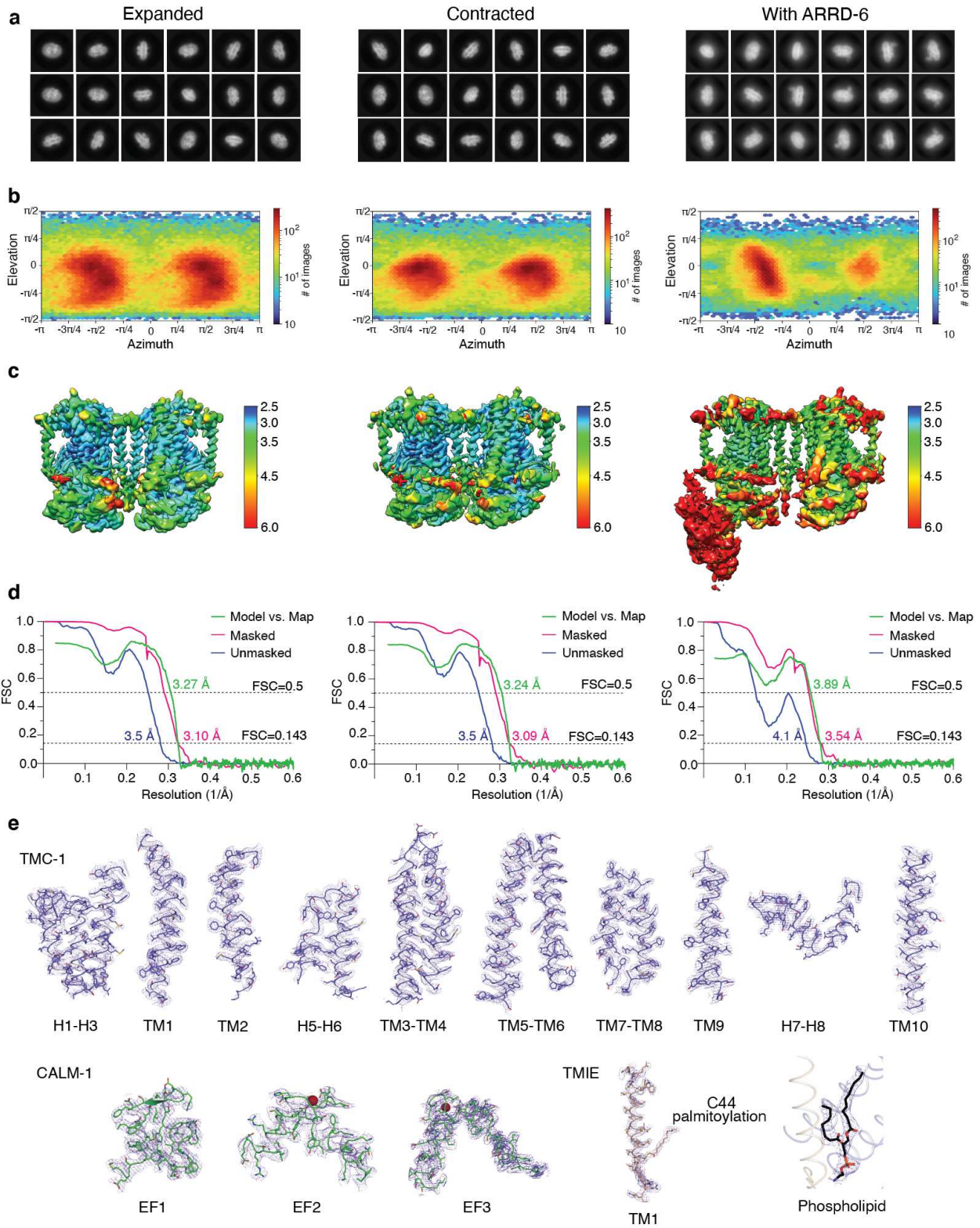


996

997 **Extended Data Fig. 4. Cryo-EM processing workflow of TMC-1 complex with ARR-6.**

998 Flow chart for cryo-EM data analysis of the TMC-1 complex with ARR-6.

999

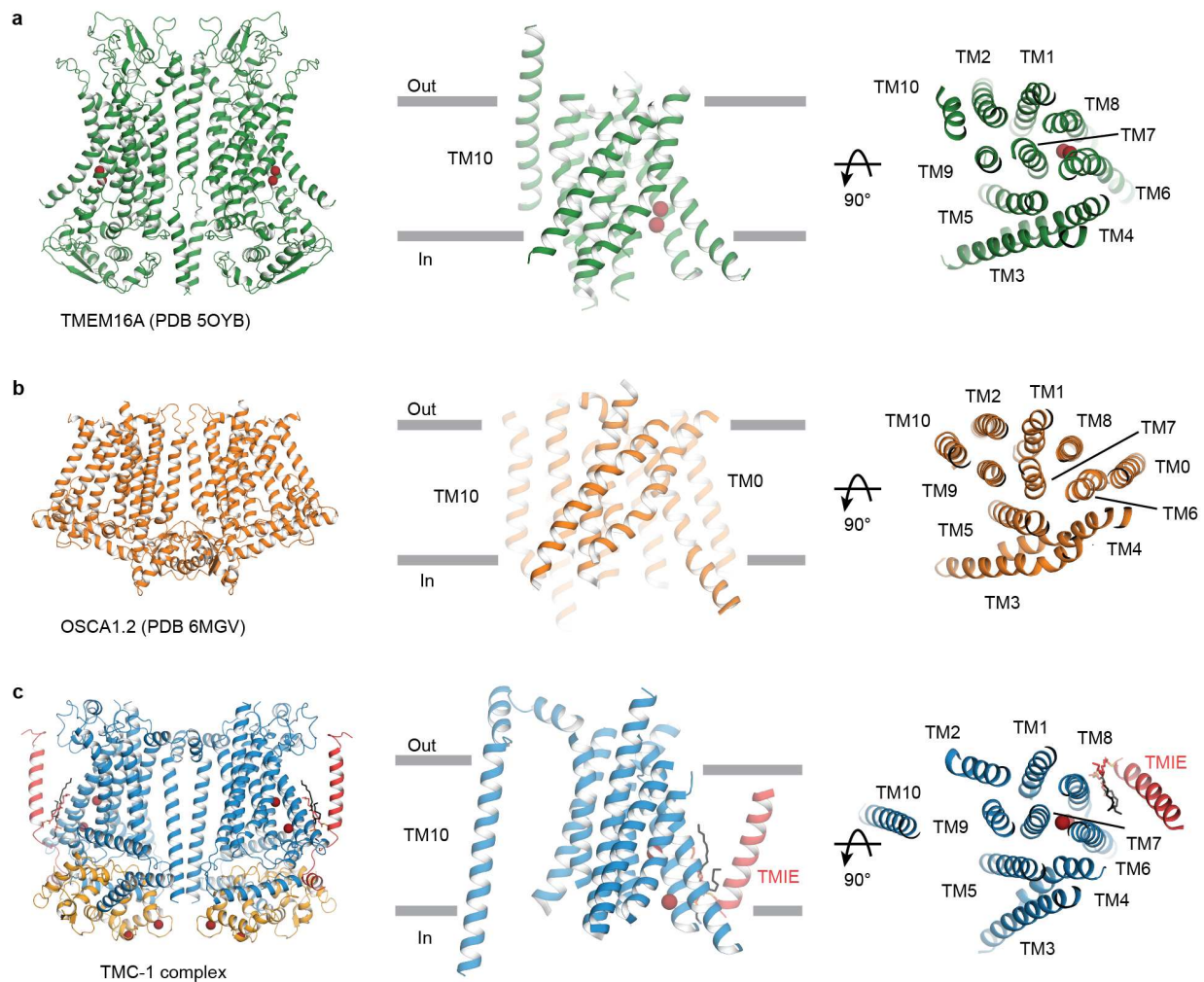


1001 **Extended Data Fig. 5. Cryo-EM classes, statistics, angular distributions and selected sections of**
1002 **density maps.**

1003 **a**, Selected 2D class averages of ‘E’ and ‘C’, and with ARRD-6, respectively. **b**, Angular distributions of
1004 final reconstructions. **c**, Electron density map of each model colored by local resolution values. **d**, Fourier
1005 Shell Correlations (FSC) curve for each model. **e**, Fragments of cryo-EM density map and atomic model of
1006 each auxiliary subunit. The cryo-EM maps are shown as purple mesh.

1007

1008



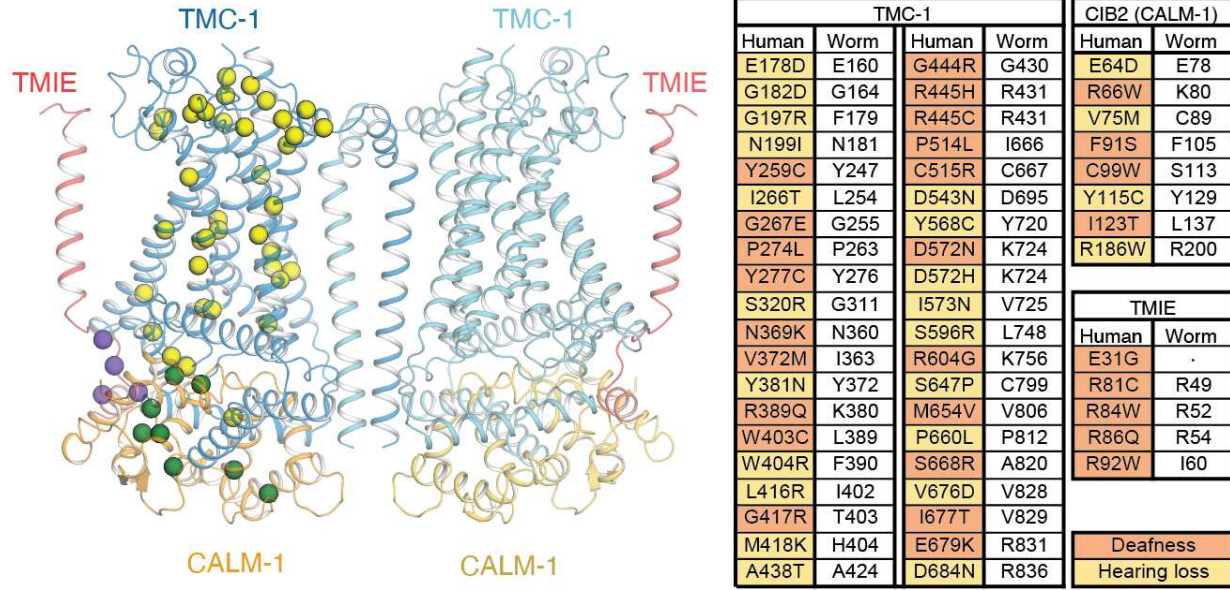
1009

1010 **Extended Data Fig. 6. Structural comparison of TMEM16, OSCA1.2, and the TMC-1 complex.**

1011 **a, b, c.** Structures of TMEM16A (5OYB), OSCA1.2 (6MGV), and the TMC-1 complex viewed from the
 1012 same relative perspective. The side view of the transmembrane regions and the top-down views are shown
 1013 in the cartoon model. Putative ions are shown as red spheres.

1014

1015



1016

1017 **Extended Data Fig. 7. The locations of key mutations mapped to one protomer of the TMC-1 complex.**

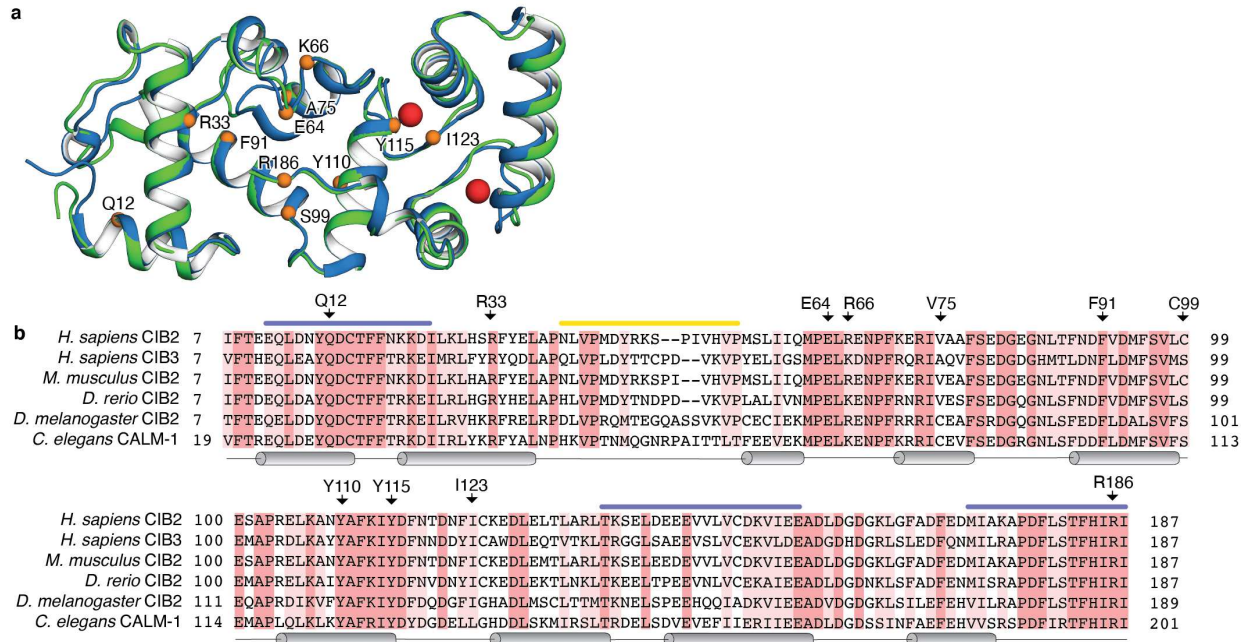
1018 The structure of the TMC-1 complex and the locations of mutations causing either hearing loss or deafness.

1019 α positions of the residues in question are shown as yellow (TMC-1), green (CALM-1), or purple (TMIE)

1020 spheres.

1021

1022



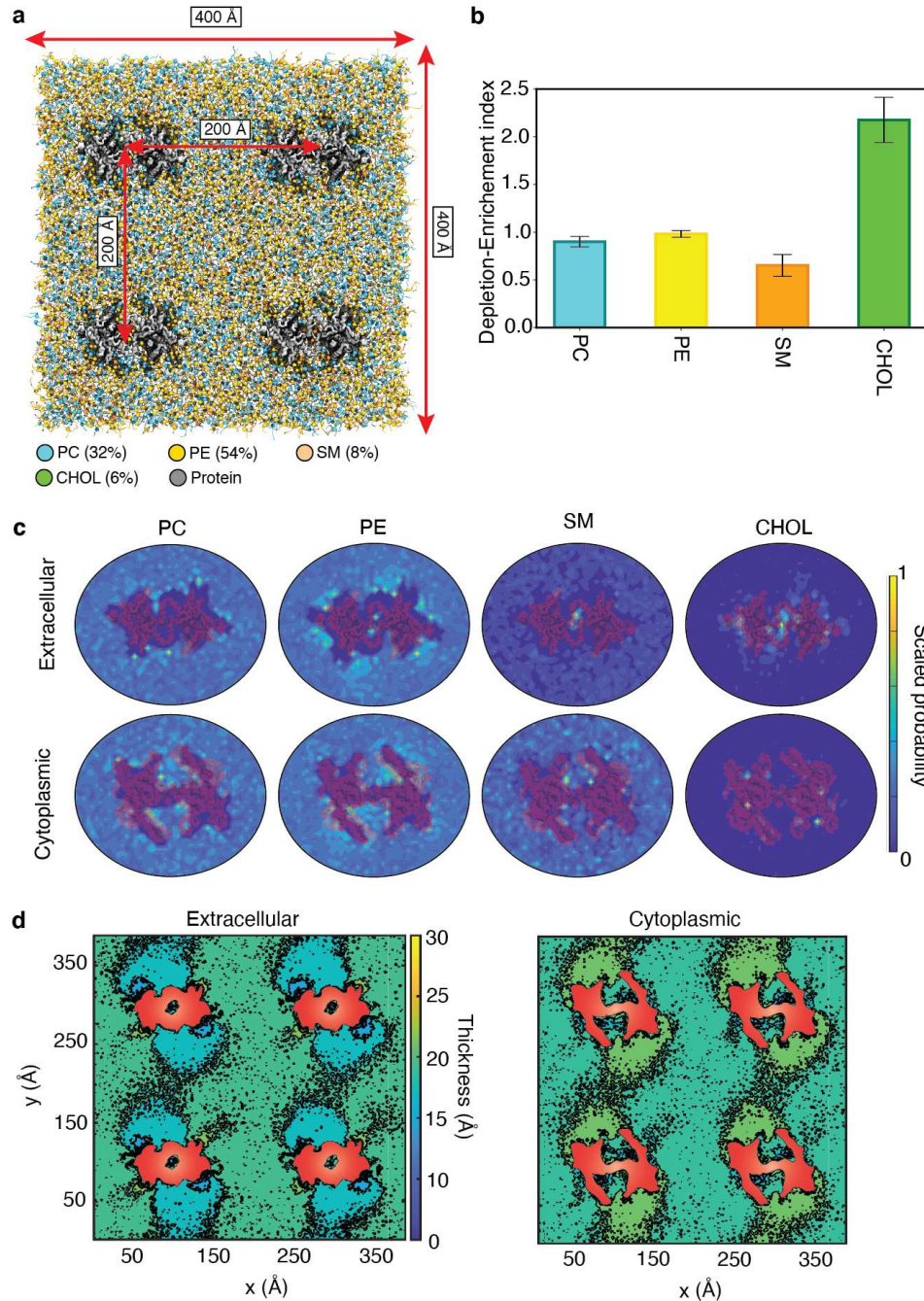
1023

1024 **Extended Data Fig. 8. Structural and sequence alignment of CALM-1, CIB2, and CIB3.**

1025 **a.** Superposition of *C. elegans* CALM-1 (green) and human CIB3 (blue, PDB 6WUD) using backbone α -
 1026 carbon atoms highlights structural conservation (RMSD = 0.7 Å). Calcium (CALM-1) and magnesium
 1027 (CIB3) ions are shown as red spheres. CIB2 residues implicated in deafness or hearing loss mutations are
 1028 shown as orange spheres. **b.** Sequence alignment of human CIB2, human CIB3, and CIB2 orthologs from
 1029 mouse, zebrafish, fly, and worms. Identical residues are highlighted in red and similar residues are
 1030 highlighted in pink. Regions involved in interactions with TMC-1 are depicted as blue bars and the region
 1031 of ARRD-6 interaction is shown as a yellow bar. Secondary structure elements are shown below the
 1032 sequence and the location of human CIB2 deafness mutations are indicated above the sequence.

1033

1034



1035

1036 **Extended Data Fig. 9. Coarse-grained MD simulations of TMC-1 complex in a membrane bilayer. a,**

1037 Four TMC-1 complexes (gray) in the 'E' conformation embedded in a lipid bilayer composed of PC, PE,

1038 SM, and cholesterol (CHOL) shown in cyan, yellow, orange, and green, respectively, with a molar ratio of

1039 32:54:8:6. **b,** Enrichment-depletion index of each lipid component in the proximity of the protein. PC and

1040 PE densities in the bulk and in proximity of the protein are similar, whereas SM is depleted and CHOL is

1041 enriched in the vicinity of the protein relative to their bulk concentrations. **c**, Heatmaps representing
1042 distributions of different lipid species around the protein. Each distribution is calculated for the last 4 μ s of
1043 the trajectory and averaged over all 4 protein replicas. **d**, Lipid bilayer thickness calculated for the
1044 extracellular and cytoplasmic leaflets averaged over the last 4 μ s of the trajectory. The cross-section of the
1045 protein is shown in red. The color scale represents the thickness of each leaflet with blue and yellow
1046 corresponding to thinning and thickening, respectively.

1047

1048 **Extended Data Table 1 Statistics for 3D reconstruction and model refinement.**

States Codes	Expanded (EMD-26741) (PDB 7USW)	Contracted (EMD-26742) (PDB 7USX)	With ARRD-6 (EMD-26743) (PDB 7USY)
Data collection and processing			
Microscope	Titan Krios		
Camera	K3 BioQuantum		
Magnification	105,000		
Voltage (kV)	300		
Defocus range (μm)	-1.0 to -2.4		
Exposure time (s)	3.329		
Dose rate ($e^-/\text{\AA}^2/\text{s}$)	14.9		
Number of frames	50		
Pixel size (\AA)	0.831 (0.4195; Super-resolution)		
Micrographs (no.)	25,852		
Initial particles (no.)	3,216,845,		
Symmetry imposed	C2		C1
Final particles (no.)	142,396	140,559	99,248
Map resolution (\AA)	3.10	3.09	3.54
FSC threshold	0.143	0.143	0.143
Refinement			
Initial model (PDB code)	De novo, Alphafold2, 6WUD		Expanded
Model resolution (\AA)	3.27	3.24	3.89
FSC threshold	0.5	0.5	0.5
Model composition			
Non-hydrogen atoms	14,322	14,220	16,582
Protein atoms	13,552	13,544	16,364
Ligand atoms	770	676	218
<i>B</i> factors (\AA^2)			
Protein	46.17	55.26	65.34
Ligand	40.03	44.20	9.06
R.m.s. deviations			
Bond length (\AA)	0.003	0.003	0.003
Bond angle ($^\circ$)	0.511	0.546	0.649
Validation			
Favored (%)	96.87	96.25	97.01
Allowed (%)	3.13	3.75	2.99
Disallowed (%)	0	0	0
Poor rotamers	0	0	0
MolProbity score	1.59	1.53	1.64
Clash score	7.32	6.20	8.74

1049

Supplementary Files

This is a list of supplementary files associated with this preprint. Click to download.

- [SupplementaryInformation.pdf](#)